2009

The effect of near-surface metallurgy on the machinability of cast iron

William Dewey Peach

THE EFFECT OF NEAR-SURFACE METALLURGY ON THE MACHINABILITY OF CAST IRON

by

WILLIAM DEWEY PEACH

A THESIS

Presented to the Faculty of the Graduate School of the

MISSOURI UNIVERSITY OF SCIENCE AND TECHNOLOGY

In Partial Fulfillment of the Requirements for the Degree

MASTER OF SCIENCE IN METALLURGICAL ENGINEERING

2009

Approved by

Von L. Richards, Co-Advisor
Kent D. Peaslee, Co-Advisor
Frank Liou, Committee Member

ABSTRACT

The increasing performance and durability of cutting tool inserts have created metallurgical challenges for production foundries to produce near-net shaped castings within strict dimensional tolerances. In order for foundries to take full advantage of the increased cutting speed capabilities, it becomes necessary to reduce machining allowances and produce much more stable casting surfaces. To accomplish this, a better understanding of the complex microstructures formed within the first 0.120 in. (3 mm) of the mold/metal interface (as-cast surface) is necessary. The goal of the work presented here was to examine the microstructures formed in the near-surface region of gray iron castings, determine what was responsible for formation, and how these microstructures behaved during the machining process. A series of experiments were performed to evaluate the effect of graphite flake morphology, matrix microstructure, and alloying elements on near-surface machinability. Three-dimensional cutting forces, quantitative metallography, and high-speed photographic measurements were used to evaluate the behavior of flake graphite, ferrite, coarse/dense pearlite, steadite, and carbides during the machining process. Data from the experiments also indentified the importance of inoculation practice, cooling rate, and mold sand properties on the final near-surface microstructure/machinability behavior. A case study was then performed for industrial brake rotor castings produced from class 35 gray cast iron, in which diagnosis of a machinability problem proved to be near-surface microstructure related. It was found that a combination of mold sand properties and inoculation practice were responsible for surface free-ferrite/graphite morphology microstructural defects.

ACKNOWLEDGMENTS

This work would not have been possible without the knowledge, guidance, support, and patience of Dr. Von Richards, Dr. Kent Peaslee, Dr. Liou, and Dr. Simon Lekakh. From whom I was given the chance to learn metallurgical fundamentals, the scientific testing approach, statistical data analysis, and to critically think before making a research decision. Special thanks to Jack Jones, Nathan Inskip, and Jimmie Taylor II for their experience, instruction, and advice. From them I learned how to safely operate a wide range of machining equipment more efficiently and to troubleshoot machining difficulties. Additional thanks goes to Jared Teague, Hank Rawlins, and Valerie Jamerson for much assistance and many suggestions. The author would also like to thank the AFS 5H – Gray Iron Research Committee and AFS 5I – Ductile/CG Iron Research Committee for oversight and input as well as funding provided through AMC's Casting for Improved Defense Readiness (CIDR) program sponsored by the Defense Logistics Agency (DLA) through the Advanced Technology Institute (ATI). For co-sponsorship and permission to perform plant trials thanks to Dalton Foundries and Asama Coldwater Manufacturing as well as the foundries that responded to the AFS sponsored industrial machinability survey.

TABLE OF CONTENTS

LIST OF ILLUSTRATIONS

Page

LIST OF TABLES

Page

1. INTRODUCTION

1.1. BACKGROUND

1.1.1. Purpose of Research. The increasing performance of machining tool inserts has presented casting producers with an opportunity to greatly increase productivity while reducing machining costs. Cemented-carbide and mixed oxide-ceramic inserts are capable of machining at much higher cutting speeds than traditional tool steels while maintaining much longer tool lifetimes. New tool designs can be produced with superior hardness, fracture toughness, and high-temperature wear characteristics, much to the satisfaction of the foundry machinist. However, as the demand for high speed machining tools increases, challenges are passed onto the casting producer to create castings with more tightly controlled geometrical/dimensional tolerances and consistent surface microstructures. In order to take full advantage of these new tooling technologies, metallurgists need to understand several engineering obstacles related to both metals casting and machining methodologies.

The goal of this work was to characterize and quantify the effects of near-surface metallurgy on the machining behavior of gray cast iron test articles modeled after brake rotor castings. With a better understanding about how the near-surface (as-cast surface) microstructures develop and behave during the machining process, reductions to machining allowance can be made, thereby increasing tool lifetimes and productivity.

1.1.2. Machining Allowance and Common Machining Practice. Machining allowance is additional material deliberately added to a casting design to account for dimensional variations during the casting process as a result of metal shrinkage, mold/metal interactions, and feature misalignment across the mold parting line. Casting producers must remove the machining allowance from each casting in order to meet dimensional tolerance and surface property requirements specified by the customer. Both ASME Y14.5M and ISO 8062-3 standards are used to ensure that all dimensions of the castings supplied by the casting producer are within agreed limits (i.e. +/- 0.005”). These standards also provide machining recommendations with regard to the material, casting

method, and complexity of the part produced. For gray cast iron parts produced in green sand molds there are three machining allowance grades with material additions ranging 0.040” to 0.060” (1 mm to 1.5 mm) per surface [1]. The machining allowance level is selected based on the number of parts produced, capabilities of the casting producer, complexity of finished surface texture, and cost.

For machining stock removal in brake rotor production the most commonly used machining operation is referred to as facing, a variation of the single point turning process. The facing process is normally performed in a computer numerically controlled (CNC) lathe and a representation is shown below in Figure 1.1. In a facing operation the workpiece (casting) is rotated about a central axis (Z) which dictates the cutting speed (V), a cutting tool is then brought into contact with the workpiece face (A to B), and travels along a single axis (X) toward the center of the casting with a feed rate (f). A depth of cut (DOC) is specified as a measure of material removal, represented in Figure 1.1 by a dashed line.

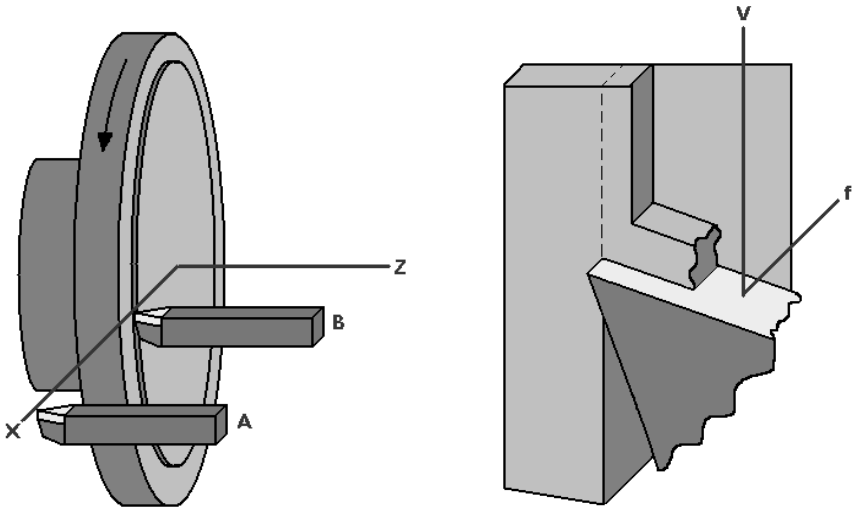

Figure 1.1: In Facing the Tool (at Point A) Travels Along the X-Axis with a Feed Rate (f) Toward the Central Axis of Rotation (Z). Cutting Speed (V) is Controlled by Rotation

Two specialized facing operations are used to remove the machining stock from gray iron brake rotor castings. The first is referred to as a “roughing” cut and consists of

using a large nose radius cutting tool to remove 0.030” to 0.150” (~0.8 mm to 4 mm) of the as-cast surface [2]. This procedure is performed to remove the near-surface geometrical and microstructural inconsistencies from the casting as well as those associated with machining tooling set-up or workpiece installation. Following the rough machining operation, a “finishing” cut is performed in which as little as 0.0001” (0.0025 mm) is removed from the surface [3]. The finishing pass is used to accurately reduce the casting size to its final dimensions and more importantly to impart the final surface quality (surface finish) before further processing.

The machining parameters of cutting speed, feed rate and depth of cut are selected for optimization of both tool life and machining time. The most common method for selecting a set of machining conditions is based on the casting’s brinell hardness number (BHN) and whether machining will be performed with or without a coolant. For gray cast irons, and more specifically brake rotor castings, machining is typically performed without coolant due to the superior hot hardness of cemented-carbide tools over that of tool steel cutting tools traditionally used in the past. Furthermore, environmental concerns surrounding cooling fluids have caused many toolmakers to focus on producing self-lubricating tools or to recommend compressed air-cooling [4].

1.2. REVIEW OF LITERATURE

1.2.1. Chip Formation. The machining process utilizes a cutting tool’s edge to severely plastically deform and shear away unwanted material through a process of chip formation. Figure 1.2 presents a traditional diagram of a machine chip forming in which a tool with a specified depth of cut moves across a workpiece surface. The material ahead of the advancing tool experiences elastic compression until it reaches the primary shear zone. The material then experiences a large amount of sudden plastic deformation, activating dislocation movement and subsequent dislocation tangling resulting in work-hardening. The loss of ductility due to work-hardening within the shear zone causes the material to shear along the shear plane, form shear step discontinuities, and move up the

rake face of the cutting tool to form a machine chip [4-6]. It is important to note that although the shear plane is commonly defined by a single angle (Φ), in reality shearing of the chip material occurs through a larger consistently changing region. In addition to the primary shear zone a region of secondary shear zone forms along the rake face of the cutting tool and grows in thickness as the cutting speed increases. Significance is given to point A because this is where the forming chip separates from the cutting tool face.

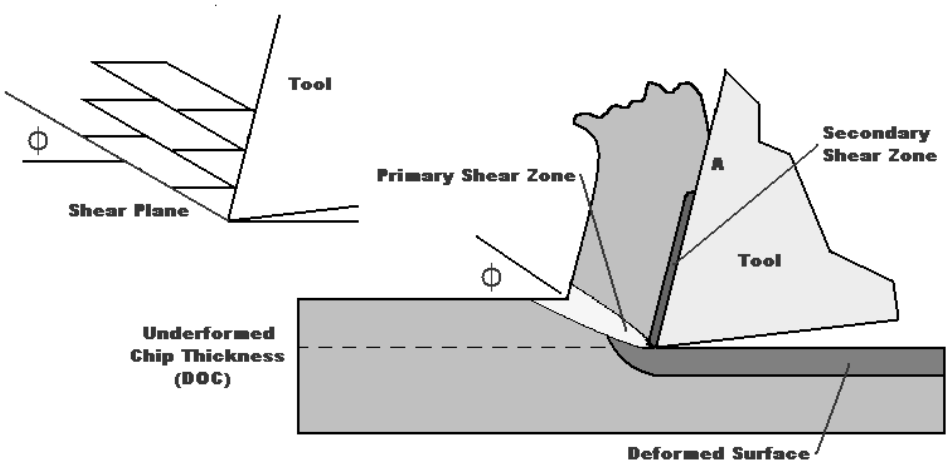

Figure 1.2: Deformation Diagram of Chip Formation

In 1938 Ernst studied the physics of chip formation in metals and described three major chip formation phenomena. Ernst found the ductility of the material determined the chip type: discontinuous, continuous, or continuous with build-up edge (BUE). Figure 1.3 depicts the chip formation mechanisms studied by Ernst. When machining gray cast iron, the mixture of brittle (pearlite) and ductile (ferrite) microconstituents caused the chip formation characteristics to exhibit all three mechanisms. Further research showed that both the microstructure as well as the machining parameters had a large effect on the chip formation mechanism [7]. By 1954, Shaw had discovered that the machining parameter of cutting speed was also a factor in the chip formation mechanism [8]. Researchers through the 1950's believed that the machine chip curled away from the tool face as a result of wearing of the tool [10]. In 1963, Cook proposed

relationships between chip formation and tool wear contrary to the current theories. Cook suggested that the machine chip curling away from the rake face of the tool was responsible for tool wear and studied the stress distribution within in the chip under different cutting speeds [3]. In 1970, it was found that BUE occurred in the presence of both discontinuous and continuous chips, at which point BUE as a chip formation mechanism was re-evaluated as a tool wear phenomena [9].

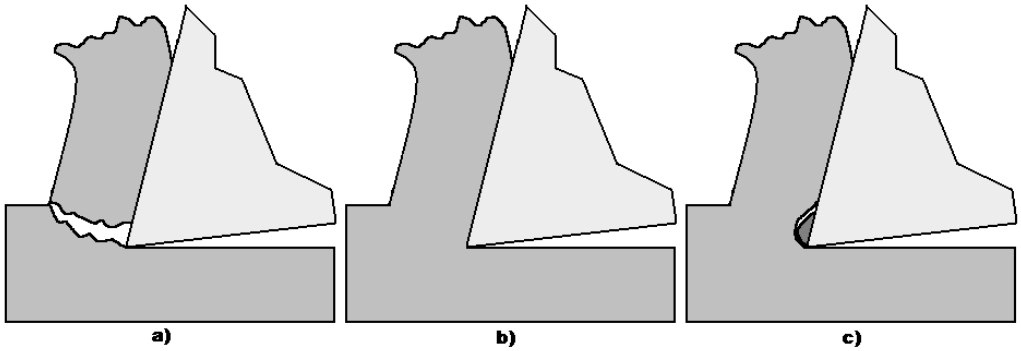

Figure 1.3: Mechanisms of Chip Formation: a) Discontinuous, b) Continuous, and c) Continuous with Build-Up Edge

In recent years a number of researchers have began to re-investigate machining fundamentals using modern technology with the intent to redefine machinability. Work performed by Voight and Marwanga studied the behavior of gray cast iron (GCI) ahead of the cutting tool using a quick stop device and an ultra-high speed video camera. Figure 1.4 illustrates the three distinct regions (or machine affected zones, MAZ) found to exist in the gray cast iron microstructure: a decohesion zone, fracture zone, and shattered zone. In the de-cohesion zone graphite flakes were found to break and separate from the matrix microstructure. The fracture zone was characterized by fractures extending from the shattered zone into the decohesion zone, following the path created by the separated graphite flakes. Finally, the shattered zone consists of angular particles that make up the discontinuous chips which flow up the rake face of the cutting tool [10].

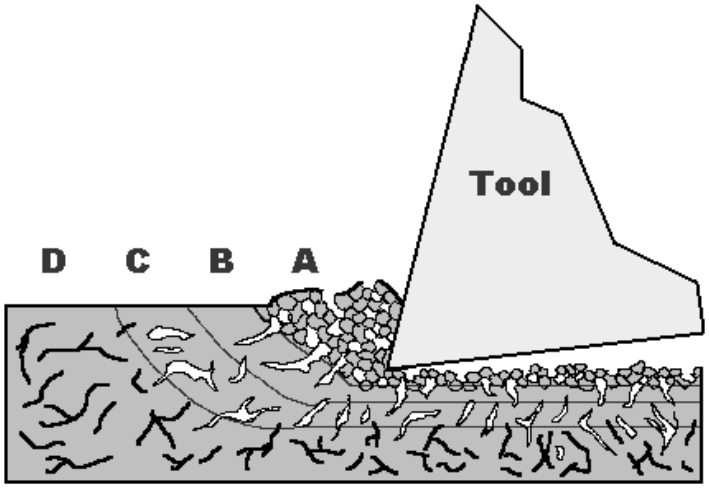

Figure 1.4: Machine Affected Zones: a) Shattered Zone, b) Fracture Zone, c) Decohesion Zone, and d) Unaltered Zone

In addition to a better understanding of the chip formation process, the significance of machining research was that chip formation behavior was tied directly to that of tool wear and machinability. Improvements in tool materials along with the desire for higher cutting speeds led to researchers taking a more microscopic look at tool wear mechanisms and the cutting conditions responsible.

1.2.2. Tool Wear. Four wear mechanisms are present in the machining process: abrasion, adhesion, corrosion, and fatigue. Specific types of tool wear are made up of a combination of the wear mechanisms and classified by the location where they occur on the tool insert, as shown in Figure 1.5 [11]. There are two main locations of wear in the turning process: flank wear and crater wear. Flank wear is primarily attributed to abrasion due to contact between hard phases in the workpiece material and the cutting edge of the tool insert. As flank wear on the tool edge increases the cutting surface changes resulting in a loss of dimensional control, an increase in heat generation, and a reduction in surface finish quality [5]. The majority of flank wear occurs near the casting surface where the tool edge is more likely to encounter entrapped sand grains and harder carbide/pearlite phases due to mold/metal interaction or rapid solidification. For cast irons, the abrasive nature of flank wear has been found to be dominant at lower cutting speeds (below 1000 surface feet per minute, sfpm or 300 surface meters per minute,

smpm) [6]. Minimal abrasion wear occurs on the rake face of the tool, except near Point A in Figure 1.2 where the secondary shear region ends. As the chip material passes Point A it begins to curl away from the tool due to residual compression of the chip material opposite the tool face as a result of high shearing strains [5]. The location of Point A on the rake face of the tool is not fixed and shifts therefore resulting in abrasion wear.

As cutting speeds increase, crater wear resulting from material build-up and diffusion begin to provide the majority of tool wear. Crater wear occurs on the rake face away from the edge of the tool where cutting temperatures are the highest. It forms when successive layers of strain-hardened workpiece material adhere to the tool surface, giving rise to the secondary shear zone in Figure 1.2. This strain hardened and successive layered material was found to be the build-up edge (BUE) phenomena described in the cutting studies performed by Ernst. The BUE material does not move up the rake face of the tool as quickly as the rest of the chip material [7]. The reduced movement causes the BUE material to remain in contact with the tool material for longer at high temperatures accelerating wear by diffusion. At a critical point the accumulating layers of BUE material become unstable, break off, and are carried away with the chip material. BUE break off coupled with diffusion at elevated temperatures is responsible for crater wear and ultimately tool failure if left unchecked.

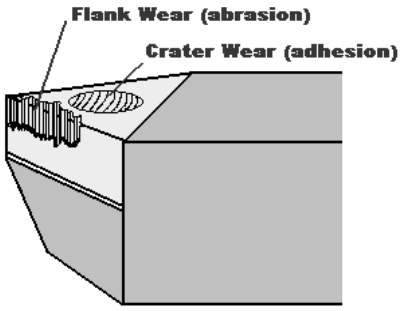

Figure 1.5: Comparison Between Flank and Crater Wear

1.2.3. Definition of Machinability. Machinability can be simply defined as the performance of a material during the machining process. However, in reality machinability is a complex quantity resulting from the sum of interactions between numerous variables, many of which are specifically dependent on the machining operation. As a result the methods of measuring machinability are widely varied and not always directly comparable. For example in the turning process machinability can be based on the number of castings machined before a predetermined amount of tool wear, the roughness of resultant surface finish, the magnitude of measured cutting forces, etc. Furthermore, the machinability behavior of a material is affected by the cutting parameters used (i.e. cutting speed, feed rate, depth of cut). Therefore, in order to better understand the machinability of a given material various definitions are typically grouped by dependence on material properties, tool properties, and cutting properties [7,12]. The list below shows some of the traditional variables and procedures that have been to quantify machinability.

MATERIAL PROPERTIES	TOOL PROPERTIES	CUTTING PROPERTIES
Specific Cutting Energy (u, k)	V_{30} tool life (ISO 3685)	Cutting Forces ($F_{cutting}$, $F_{passive}$, F_{normal})
Specific Horsepower	Rate of Metal Removal	Surface Finish (R_a, R_z,)
Shear Stress		Machine Chip Morphology
		ASTM E 618-81

The methods used in this study focused on the material and cutting property definitions of machinability. Specifically the variables of specific cutting energy, cutting forces, and surface finish were considered with an additional investigation performed to quantitatively evaluate chip shape. These variables were chosen due to the large amount of data that could be generated from a limited number of castings (< 20 castings per heat). The requirements of the tool property definitions of machinability were found to be difficult to meet in the laboratory setting due to the large number of castings required to test them. Typically, tool property definitions are used in foundries where 50+ castings produced from a single heat are machined and the machinability tracked on a heat to heat basis.

1.2.4. Development of Machinability Testing. Fundamental work regarding the machinability of metals was performed in 1906 by Taylor in which tool life was related to cutting speed by:

$$VT^n = K \tag{1}$$

Where V refers to the cutting speed, T refers to tool life, and the constants (n and K) are empirically determined [14]. Further modifications to Taylor's equation led to the addition of feed rate and depth of cut variables, as well as additional empirically determined constants. However, two problems were recognized with the Taylor equation: 1) only expected tool life could be calculated and 2) machining parameters significantly influenced the experimentally determined constants. In an effort to standardize the large amount of data from machinability research the machinability index (M) was created. In this system all materials were compared to a standard fixed-pressure turning operation using cold-drawn B1112 steel workpiece material, high-speed tool steel cutting inserts, and a cutting speed of 180 surface feet per minute (sfpm) [15]. In 1956 Moore and Lord investigated the effects of microstructure on the machinability index and developed an equation specifically targeted toward gray cast iron [15].

$$M = 195.5 - 1.26 \cdot V_{vp} + 11.7 \cdot V_{vg} + 1.26 \cdot S_g \tag{2}$$

Where V_{vp} and V_{vg} refer to the volume fractions of pearlite and graphite in the microstructure, respectively. S_g is determined by the average size of the graphite flakes in microns. In a similar manner to that of Taylor's equation, the machinability index was found to become less reliable as ceramic cutting tools improved and as a result machinability research began to focus on tool wear/cutting force relationships [3,17,18].

Despite losing accuracy due to rapidly developing tooling materials the machinability index still remains a proven means of first approximation when choosing machining parameters. To further refine machining operations some researchers have begun to develop specialized techniques involving numerical modeling and real-time acoustic/vibration analysis. Eleftherios in 1996 developed a method for evaluating

machinability and tool lives by solving machining parameter optimization models using real-time data collection devices [19]. The solutions of these numerical models were then directly input into a computer controller to modify the machining parameters on-line. Furthermore, Kozochin and Kochinev in 2006 showed that it was possible to identify near-surface microstructural variability, work hardening, and changes in surface finish/dimensional accuracy by analysis of machining acoustics [20].

1.2.5. Cutting Forces and Specific Cutting Energy. Cutting forces are measured using multiple dynamometers (strain gauges or piezoelectric load cells) which are installed into a cutting tool holder. The dynamometers measure deflections in the tool holder, from which three dimensional cutting forces at the tool can be calculated [21]. A diagram depicting the placement of dynamometers and the forces experienced by a tool holder is shown below in Figure 1.6. The main cutting force (F_c) and feed force (F_f) act parallel to the cutting and feed rate directions, respectively. Both the main cutting force and the feed force are primarily influenced by the hardness of the workpiece. The normal force (F_n) measures the contact force attempting to push the tool holder back away from the workpiece.

Beginning in the mid 1990's researchers found that ratios between the various cutting forces can provide information about machinability and the extent of flank wear that has occurred. One of the more frequently used ratios is that between the feed force (F_f) and the cutting force (F_c). These ratios are extremely useful because rather than halting between cutting operations to measure tool wear, the cutting forces and cutting force ratios can be used to estimate tool wear continuously while machining [22]. Data can then be easily stored to provide metallurgists and machinists a valuable tool when tracking the machinability of castings on a batch by batch basis.

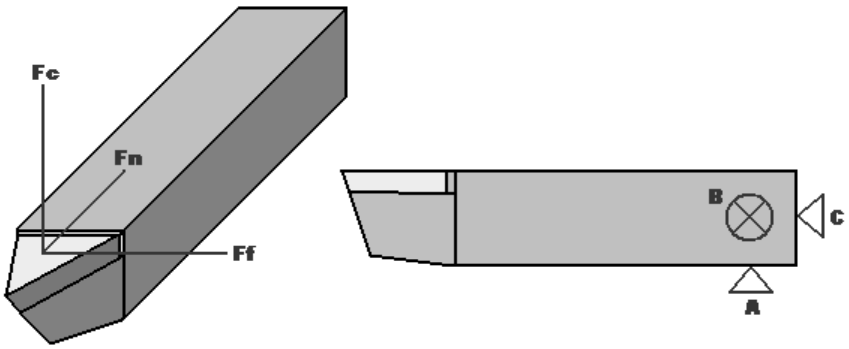

Figure 1.6: Dynamometers A, B, and C Measure Tool Holder Deflections Allowing Calculation of the Main Cutting Force (F_c), Feed Force (F_f), and Normal Force (F_n)

The major drawback with using cutting forces as a measure of machinability is that they are heavily susceptible to changes in the cutting parameters. Slight deviations in the depth of cut due to variations in as-cast surface or installation into the machining center can cause large changes in the measured cutting forces, some greater than 100 N (22.5 lb-f) [23]. To solve this problem a quantity referred to as specific cutting energy (u) was developed. Specific cutting energy is used to measure the energy required to remove a given unit volume of material with respect to the cutting parameters. The specific cutting energy equation is given by:

$$u = \frac{F_C}{t \cdot w} \tag{3}$$

Where Fc refers to the average cutting force, t is the undeformed chip thickness (depth of cut), and w is the width of the cut [24]. The specific cutting energy equation is useful because it takes into account not only tool forces, but the geometric variables associated with a machining process.

In order to use the specific cutting energy equation in the turning/facing process it is necessary to modify the parameters slightly because the width of cut is a dynamic quantity controlled by the feed rate. Therefore, the specific cutting energy coefficient (k) equation was developed:

$$k = \frac{F_C}{f \cdot t} \tag{4}$$

Where F_c refers to the average cutting force, f is the feed rate, and t is the depth of cut. By maintaining a constant feed rate and assuming proportionality between the cutting forces and depth of cut it is possible to use the specific cutting energy coefficient equation to examine how depth of cut from the as-cast surface affects cutting forces and machinability. This is useful because it allows casting producers a way to test how changes to the casting process directly affect machinability and the efficiency of the turning process regardless of the casting dimensions.

1.2.6. Surface Finish. For machining operations where it would be impractical to continuously measure/record cutting tool forces, the quality of the finished surface can indicate a great deal about the machinability of a casting. The surface finish of a casting after machining is highly dependent on the chip formation mechanism, microstructure (hardness) of the workpiece material, and performance of the cutting machine. For single point turning low cutting speeds and discontinuous chip formation lead to scalloped or cracked surfaces, higher speeds with unstable BUE lead to regions of adhered BUE fragments on the new surface, and higher speeds without BUE or stable BUE result in low roughness values. When a workpiece is improperly secured during a machining operation "chatter" and vibrations during the cutting process can be evident on the newly machined surface. Figure 1.7 below offers an illustration of the various surface conditions after machining [5].

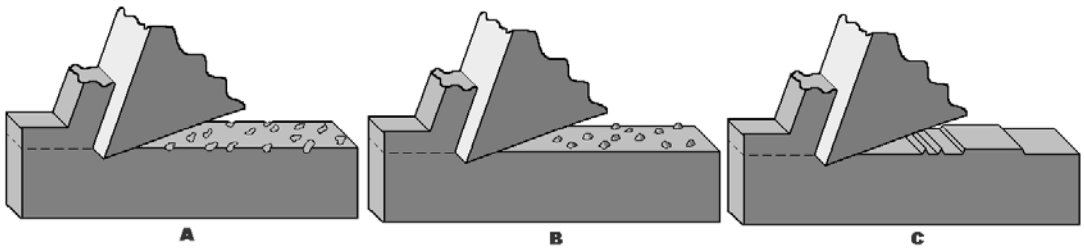

Figure 1.7: Chip Formation Characteristics can Impact the Machined Surface Quality: a) Discontinuous Chips, b) Unstable BUE, and c) Machine Chatter

In order to quantitatively measure the surface roughness of a casting surface, the quantities of average arithmetic surface roughness (R_a) and average distance between highest and lowest points per sampling length (R_z) are commonly used. The ideal average arithmetic surface roughness (R_a) can be calculated prior to machining if the feed rate (f) and nose radius (R) of the cutting tool insert are known:

$$R_a = \frac{f^2}{32 \cdot R} \tag{5}$$

Calculations involving the actual R_a and R_z values of a casting utilize equations 6 and 7 below. The surface data used in the equations is collected using a hand-held stylus profilometer or stationary laser/optical profilometer with a fixture. Regardless of the method used to collect the surface data the device stores a series of data points that are used to generate a surface profile.

$$R_a = \frac{1}{n}\sum_{i=1}^{n} y_i \tag{6}$$

$$R_z = \frac{1}{s}\sum_{i=1}^{s} R_{ti} \tag{7}$$

Where n is the number of data points collected, y_i is the height of the ith measured data point on the surface profile, s is the number of sampling lengths, and R_{ti} is the maximum height of the surface profile (the difference between the highest and lowest point) over the ith sampling length

One of the major difficulties when using the surface finish to define the machinability of a casting is that the roughness can be influenced by the “flatness” of a surface as well. Flatness refers to the difference in height between opposite ends of a measured surface profile. An illustration of the difficulties associated with flatness can be seen below in Figure 1.8. In the diagram flatness begins to affect the measured surface roughness when the underlying geometry of the casting either increases or

decreases the actual surface profile in a specific location. The majority of flatness variations are observed in stationary profilometer systems when a fixture is used as opposed to a hand-held device that can be oriented according to the underlying casting features.

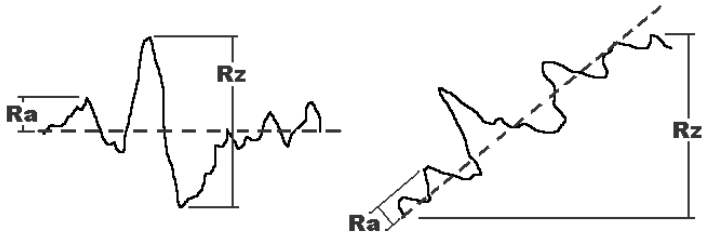

Figure 1.8: Effect of Underlying Surface Flatness on Ra and Rz Values

1.2.7. Chip Morphology. The morphology of the machining chip can provide a significant amount of data about the machinability behavior of a material without measuring cutting forces or surface roughness. In the turning process the undeformed chip thickness is specified as the depth of cut and by measuring the deformed chip thickness it is possible to compare machinability using the chip-thickness ratio (r):

$$r = \frac{t}{t_C} = \frac{\sin(\Phi)}{\cos(\Phi - \alpha)} \tag{8}$$

Where t is the undeformed chip thickness (depth of cut), t_c is the chip thickness after machining, Φ is the shear plane angle, and α is the rake angle (the angle between the rake face of the cutting tool and a plane perpendicular to cutting surface). The importance of the chip-thickness ratio is that if the rake angle, depth of cut, and chip thickness after cutting are known the angle of the shear plane can be calculated [7,25].

1.2.8. Formation of Gray Cast Iron Microstructures. Gray cast iron (GCI) is the name given to iron alloys containing between 2.5 to 4% C and 1 to 3% Si in which soft graphite flakes are present throughout the matrix microstructure. Gray cast irons are classified by tensile strength (usually in ksi) which can be directly related to the final

microstructure. Due to the presence of a eutectic point at 4.3% C in the Fe-C system and the effects of alloying/tramp elements on solidification behavior, it is common to specify if an iron is hypo- or hyper-eutectic in composition. Hypo-eutectic irons (<4.3 %C) are preferred, in order to avoid weaker mechanical properties associated with the formation of massive kish graphite [26]. It is important to note, that in industry the classification of hypo-eutectic iron is based on a quantity referred to as the carbon equivalent (<4.3 %CE). In addition, added silicon and other alloys/impurities will slightly alter the positions of the eutectic temperature on the Fe-C phase diagram. The explanations in the following paragraphs deal with the pure Fe-C system, while the following section takes into account the changes due to the presence of silicon and describe in further detail the carbon equivalent.

Solidification of a hypo-eutectic iron begins with the formation of austenite dendrites, which coupled with decreasing temperature and further growth begin to increase the carbon content of the remaining liquid. With further cooling the liquid then reaches the stable iron-graphite eutectic point (2098 F, 1148 C), at which time due to over saturation of carbon in the remaining liquid both austenite and flake graphite begin to grow co-operatively as eutectic cells. In the pure iron-carbon system, approximately 10 degrees below the stable iron-graphite eutectic, a metastable iron-carbide eutectic occurs and the austenite/graphite growth is replaced by more favorable austenite/cementite formation. Upon continued cooling below the eutectoid temperature (727 C) the austenite will decompose and begin precipitating dissolved carbon. The cooling rate will then control whether pearlite, ferrite, or a mixture of both is observed in the final microstructure [27].

Even for hypo-eutectic irons that avoid kish graphite, the morphology of the graphite flake can greatly affect the mechanical and machining properties of the iron. There are five types of graphite flakes (A to E) and eight size (length) designations according to ASTM A 247. Type A graphite, with its randomly oriented flakes, is preferred due to an optimal balance between strength and wear resistance. The type of graphite flake formed is highly dependent on the solidification rate and the amount of undercooling that takes place. Type A is associated with the slowest cooling rates within the bulk of a casting, while types B,D, and E occur near the surface of the casting next to

the mold wall, where cooling rates are the quickest. Flake type C is the designation given to kish graphite and is not normally observed in the near-surface region. In extremely rapid cooling cases the formation of the stable eutectic is suppressed resulting in no graphite flakes, instead massive carbides are formed. These types of carbides (referred to as chill) are found on the edges of a rapid cooled casting or in especially thin castings [26, 28].

One useful tool for predicting the graphite flake morphology is the cooling curve, a plot of temperature from an embedded thermocouple against time. An example of a cooling curve for type A graphite is compare to a cooling curve for rapidly cooled iron that forms a chill in Figure 1.9. The temperature passes through the iron-graphite eutectic a certain amount of undercooling is required in order for graphite nucleation to become favorable, after which the heat of fusion from eutectic growth causes the overall temperature to rise (termed recalescence). If the end of solidification is reached prior to the temperature falling below the iron-carbide eutectic then the final microstructure will be free from carbides. In Figure 1.9A, cooling was so rapid that the iron-graphite eutectic was bypassed directly into the iron-carbide eutectic where the formation of carbides began. Again the eutectic formation of austenite and carbide causes the temperature to rise, in this case above the iron-carbide eutectic where graphite can begin to nucleate again. The type iron formed in this case will consist of carbide, type D or E graphite, along with both ferrite and pearlite depending on the speed through which the eutectoid temperature is passed [28].

Further increases in mechanical strength for GCI can be accomplished by increasing the number and decreasing the size of eutectic cells. This is accomplished by the addition of an inoculating agent, typically foundry grade ferro-silicon (Fe-75Si). Inoculants provide additional nucleating sites from which graphite preferentially solidifies and increase the temperatures surrounding where nucleation sites begin to grow, thereby extending recalescence locally, increasing the probability that the end of solidification is reached before the temperature falls below the iron-carbide eutectic. The other fundamental reason that inoculants are used is to promote heterogeneous nucleation. Untreated irons do not contain sufficient nucleating sites promoting homogeneous flake graphite growth. Nucleation agents act by introducing non-metallic

inclusions that act crystallographically similar to graphite. After a certain amount of undercooling the mismatch between graphite and the inclusion becomes inconsequential and the graphite begins to grow from the inclusion. Graphite additions to the melt were originally thought to provide ideal nucleating sites for graphite flakes, however the tendency for graphite to dissolve in the molten iron was high and therefore other inoculants, such as ferro-silicon containing calcium, strontium, aluminum, or barium, were identified as alternatives [29].

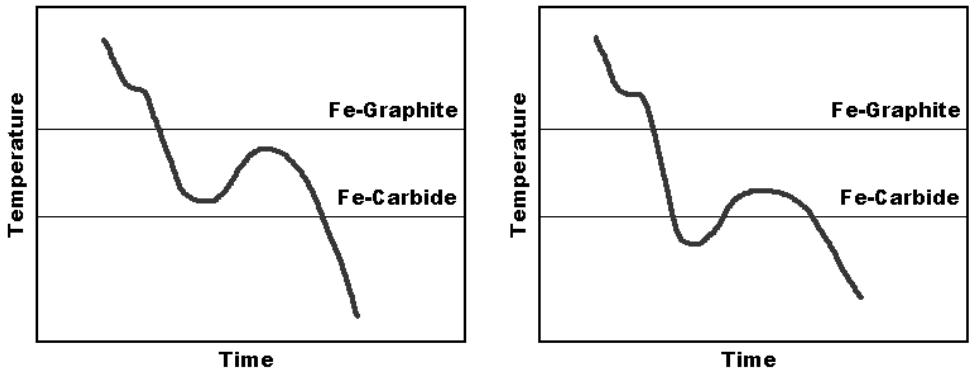

a) b)

Figure 1.9: Hypo-Eutectic Solidification of a) Type-A Graphite and b) Chilled Iron

1.2.9. Effects of Carbon Equivalent (CE). A significant amount of research over the years has been devoted to understanding how changes in the carbon equivalent affect the mechanical and microstructural properties of gray cast iron. The carbon equivalent can be represented a number of ways, the most common appearing below in equation 9.

$$CE = \%C + \frac{\%Si}{3} + \frac{\%P}{3} \tag{9}$$

where %C, %Si, and %P represent the weight percentages of the carbon, silicon, and phosphorous in the liquid melt. The carbon equivalent was first developed to account for the effects of tramp elements such as Si and P on the eutectic solidification behavior of the Fe-C system. Silicon was found to greatly widen the temperature difference between the iron-graphite and iron-carbide eutectics, as much as 86 F (30 C) at 2% Si. In Figure 1.10, the effect of Si is illustrated [28]. Other alloying and tramp elements like Cr, P, Cu, Al, Mn, Mo, etc., also alter the temperature difference between the two eutectics

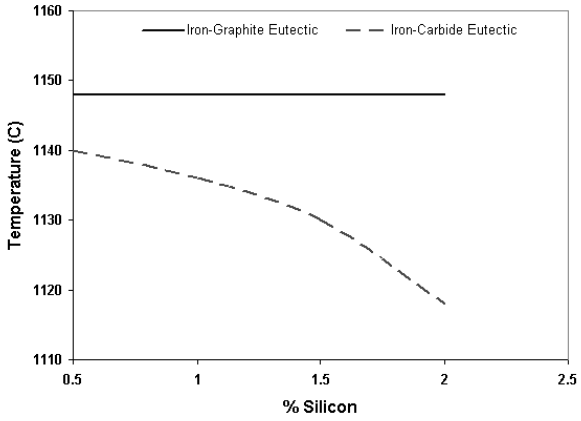

Figure 1.10: Effect of Si Content on Eutectic Temperatures

The carbon equivalent has also been directly related to approximate tensile strength and brinell hardness when the section size (cooling rate) of the casting is known. The general trend is for the tensile strength and hardness to decrease as the carbon equivalent increases due to the higher percentage of graphite formation. Increased graphite formation also increases the overall solidification time contributing to an increase in the amount of softer ferrite in the final microstructure [30].

1.2.10. Effects of Cooling/Solidification Rate. As mentioned above, with respect to graphite flake morphology the cooling rate has a significant impact on the microstructural properties of a casting. Not only can the pouring temperature (degree of superheat) affect the solidification rate, but the molding method or sand type also affects the rate. There are three main mechanisms that limit the rate of heat removed once a

casting mold has been poured: the thermal absorption of the mold, the mold/metal interface, or the heat transfer through a solidified shell. The majority of GCI is poured into sand molds, therefore the solidified thickness is limited by the mold material according to:

$$S = \frac{2}{\pi}\left(\frac{T_m - T_o}{\rho_s H_f}\right)\sqrt{K_m \rho_m C_m}\sqrt{t} \tag{10}$$

Where S is the thickness solidified, T_m is the temperature of the mold after pouring, T_o is the starting temperature of the mold, ρ_s is the density of the solidified metal, H_f is the latent heat of fusion of the metal, K_m is the thermal conductivity of the mold, ρ_m is the density of the mold material, C_m is the specific heat of the mold, and t is time. From Equation 10 it can be seen that any minor change in the molding material or pouring temperature will have a large effect on the solidification time.

The cooling rate of the casting within the mold has been found to be significantly dependent on the shakeout time and temperature. At shakeout, the casting is removed from the mold material, typically below the eutectoid temperature range 1333 F (723 C) and 932 F (500 C). In the 1970s Wallace performed a two-part comprehensive study regarding the effect of shakeout temperature on the formation of microstructures for cast irons with 4.17 to 4.62 %CE. The findings of Wallace indicated that the variety of near-surface microstructures that formed could be traced back to initial cooling rates which encompassed: mold/metal interactions, mold coatings, mold material, and inoculation practice as well as the traditional variable of pouring temperature [31, 32]. One significant finding with regard to near-surface microstructures was that sufficiently slow cooling in-mold (increased times between pouring and shakeout) resulted in a graphite free layer of ferrite “skin” 10-30 thousandths of an inch thick. Termed “free-ferrite”, this skin resulted as a consequence of short diffusion distances between small graphite flakes as castings cooled through the eutectoid reaction temperature region of the Fe-C phase diagram. Furthermore, reactions with mold coatings could increase or decrease the ferrite skin thickness, with pearl chromium (58.5% Cr, 14.8% Si, 5% C, alcohol) coatings being

the most successful form of reduction. These coatings were found to reduce the ferritic surface layer of a casting to 0.005” (0.13 mm) or less [31].

1.2.11. Effects of Phosphorous and Chrome Alloying Elements. Phosphorus (P) along with carbon, silicon, manganese, and sulfur are considered the five most common elements found in gray cast iron [1]. The presence of P in cast irons comes from the fact that traditional pig iron contains between 0.2-1.2 wt% P and that much of the scrap iron charged into the cupola or induction melters also contains between 0.05-0.5 w-t% P. Unfortunately in an iron foundry P is not an easy or cheap element to remove from a liquid metal [33–35].

Due to the complexity of the Fe-C system near the stable (graphite) and metastable (carbide) eutectic, the problem of increasing P contents in gray iron castings has been carefully studied. Much of the literature describes the effects of P on the tendency of cast irons to form an intergranular phosphide eutectic phase (steadite) and internal micro-porosity. Upon solidification the steadite phase was found to form in the last liquid to solidify between grain boundaries of the eutectic cells. Due to solute segregation in these regions just prior to solidification, the compositions of C and P in the liquid melt were found be at the highest and therefore more likely to form an iron-iron phosphide-graphite (stable) or an iron-iron phosphide-iron carbide (metastable) eutectic [36].

While a majority of the literature discusses the formation and porosity effects of steadite, few studies indicate the effect of the steadite on machinability and the final surface qualities of gray iron castings. In a response to an industrial machinability survey endorsed by the American Foundry Society (AFS), several gray iron foundries mentioned machinability problems when P levels increased above 0.09% P. Theoretically, the presence of the much harder phosphide eutectic poses problems for machinability, especially as iron foundries reduce the machining allowance of castings to reduce machining costs and produce near-net shape castings. Machining the phosphide eutectics concentrated at the grain boundaries causes the machine tool to experience rapid changes in the cutting forces (due to hardness variations), resulting in higher tool temperatures and higher tool wear rates. These elevated rates can ultimately lead to premature tool

failure/breakage and machining downtime in-house, or complaints from the casting consumer.

1.2.12. Common Near-Surface Microstructures. As a result of the interactions between the variables of alloy content, cooling rate, cooling/solidification rate, etc. described above, the near-surface region of a gray iron casting consists of a complex mixture of flake graphite, carbides, pearlite, and ferrite micro-constituents. Numerous graphite flake morphologies ranging from type E to type A are present in the near-surface region along with varying degrees of fine and coarse pearlite. In some cases graphite formation has been suppressed, leaving chill carbides present at the surface. Occasionally, interactions between the mold and molten metal during the solidification process have removed much of the carbon from the as-cast surface leaving a large amount of free-ferrite. Figure 1.11 below shows an example of the near-surface region of a gray iron casting in which pearlite, surface free-ferrite, flake graphite, and carbides can be seen.

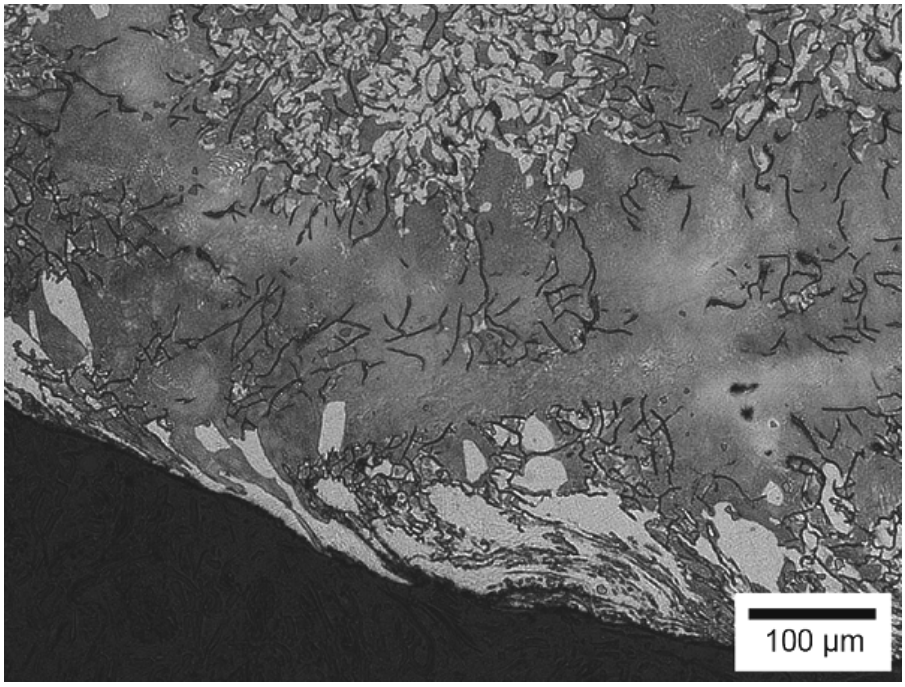

Figure 1.11: Near Surface Microstructures of Free-Ferrite (White), Flake Graphite (Black), Pearlite (Dark Grey), and Carbides (Small Angular Particles)

1.2.13. Definition and Importance of Near-Surface Machinability. Near-surface machinability is a term used to describe how the complex surface microstructures of a casting impact the cutting process. During the machining process interactions between the near-surface microstructures and surface variations cause significant variability in machinability tests (cutting forces, tool wear, etc.). As casting producers push to decrease machining allowances approaching near-net shape casting, the near-surface microstructure will no longer be completely removed by a roughing type cutting operation. As machine tools begin to more frequently pass thorough these microstructures tool wear rates will significantly increase and resultant surface finishes will degrade. Of further concern is that discontinuities of surface mechanical properties may well be present at the surface if the near-surface region is not completely removed.

1.2.14. Factors Influencing Near-Surface Machinability. There are three factors that contribute to difficulties when machining the near-surface region of a casting: the near-surface microstructures, the surface geometry, and surface defects. As described above the near-surface microstructures are the ultimate result of solidification rates and reactions that take place at the mold/metal interface. The surface geometry is dependent on roughness (before machining) and dimensional tolerances resulting from thermo-mechanical behavior of the mold materials and accuracy of parting lines of the mold halves. Finally, surface defects are the result of metal/mold interactions and improper casting design/practice. Sand burn-on is a common near-surface machinability problem in which entrapped sand grains in the surface microstructures rapidly wear the tool flank severely impacting dimensional control and machining vibration.

2. EXPERIMENTAL PROCEDURE

2.1. EXPERIMENTAL DESIGN

2.1.1. Foundry Machinability Survey. In an effort to assess the current condition of machinability problems most commonly experienced in the cast iron industry an American Foundry Society (AFS) sponsored survey was sent to gray and ductile iron foundries across the United States. The survey consisted of four sections: general classification, charge material history/melting practice, sand mold production, and machining allowance/machinability.

Foundries with monthly production ranging from 1,000 to 10,000 tons using either cupola or induction furnace melting practices were considered. The majority of foundries responding utilized a maximum of 35% steel scrap, with the remainder being a 30%/25% or a 10%/45% split of pig iron and foundry returns, respectively for initial melting. The most common alloy produced for automotive applications was found to be class 30 gray cast iron (GCI) or a D80/D100 ductile iron. 85% of the foundries responding utilized a mechanical controlled green sand system for mold production. It was found that roughly 29% of responding foundries did not track machinability, stating that it was too difficult due to the number of different parts cast and machined.
The machining allowance/machinability results indicated that the primary cause of machinability problems was the result of variations in casting hardness as a result of residual elements from the charge, deviations from established cooling rates, and casting design/section size imbalances. Specifically, problems as a result of P and Cr tramp elements in the charge materials were responsible for numerous machining problems. The results of machinability surveys were used to develop industrial and laboratory machinability tests.

2.1.2. The AFS 5J Machinability Test Article. In order to standardize machinability testing for cast irons, the American Foundry Society developed a test article (Figure 2.1) modeled after an automotive brake rotor [37, 38]. The test article consists of two sections. The first section referred to as the “hub” consists of a cylinder

2.5” (6.4 cm) tall and 3” (7.6 cm) in diameter. The second section called the “face” is a disk 1” (2.54 cm) in height and 10” (25.4 cm) in diameter. During the machinability test the hub of the test article is located in the chuck on the spindle of a lathe and a cutting tool is used to perform a series of facing operations. In this test a wide variety of variables can be measured depending on the definition of machinability chosen by the investigator.

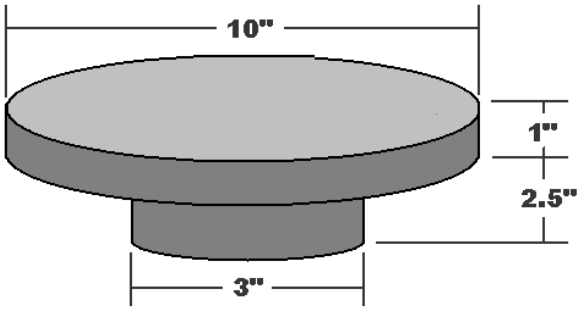

Figure 2.1: Dimensions of AFS 5J Machinability Test Article

Due to furnace capacity limitations during laboratory testing it was necessary to reduce the size of the AFS machinability test article in order to produce a statistically relevant number of test articles. To accomplish this, the machinability disk was modified. The hub of the disk was decreased to a height of 2” (5.1 cm) with a diameter of 2” (5.1 cm), while the face section remained 1” (2.54 cm) thick with a reduced diameter of 7” (17.8 cm).

2.1.3. Machining Parameters. The machining parameters used for the laboratory experiments were selected based on machining literature, foundry survey results, and laboratory lathe limitations. From empirical turning tool life data in the literature it was found that the volume of metal removed per given amount of tool wear decreased rapidly above cutting speeds of 400 sfpm in the gray cast iron system. Specifically the 300 sfpm cutting speed was chosen as an optimization between tool life and metal removal rate for both coarse and fine pearlite matrix microstructures. Cutting speed optimization was important because each of the parameters used to alter the near-

surface microstructures (cooling rates, sand types, pouring temperatures, etc.) significantly altered the pearlite spacing. Another reason for the 300 sfpm cutting speed selection was studies regarding free-carbides in the gray iron microstructure. It was found that even with up to 5% free carbides scattered throughout the casting microstructure metal removal rates behaved similarly to castings with no carbides. Between 400 to 1200 sfpm free carbides were found to cause significant decreases in tool life [2]. From the industrial surveys a major source of machinability problems resulted from inconsistencies in casting hardness. The 300 sfpm parameter was fast enough to simulate a fatigue like effect due to rapid machining through inconsistent microstructures while allowing resolution using the tool force measurement systems. Finally, a series of tests exploring the limitations of the CNC found that excessive spindle loads were experienced when the cutting speeds were increased above 400 sfpm. In a similar manner to that of cutting speed, the feed rate was set at 0.006" per revolution (0.15 mm/rev) in order to maximize metal removal rates and minimize load on the CNC spindle.

The depth of cut (DOC) was selected in order to examine the effect of microstructure variation at various depths beneath the as-cast surface. Roughing cuts were simulated using a 0.030-0.035" DOC, while finishing passes were approximated by a 0.010-0.015" DOC. The selection of a 0.035" DOC was determined to be a compromise between as-cast surface flatness and the near-surface microstructure effects. It was found that the smaller the DOC, the greater the impact of as-cast surface flatness on machinability. Larger DOC were used for specific machining operations described later in the next section, but were based on the roughing or finishing pass fundamentals.

2.1.4. Tool Force Measurement Systems. Two specific tool force measurement systems were used to capture cutting forces. A TelC DKM2010 3 component dynamometer system with a variable sampling rate up to 100 Hz was used to capture 3-dimensional cutting forces. Over the duration of an entire facing cut the system allowed for the measurement of the main, feed, and normal cutting forces.

For machinability tests where the high frequency main cutting force data was required, a custom built tool force measurement system with a sampling rate of 10,000 Hz was used. This system utilized two separate load cells (Transducer Techniques SLB-

1K) to measure both the main cutting force and passive cutting forces simultaneously. The load cells installed within a cutting tool holder were connected to a National Instruments Model 9237 Data Acquisition “full bridge” system and finally, to a laptop computer for recording. This system was also simultaneously connected to a high-frame rate InLine Model 500 video camera operating at 500 frames per second (fps). A mechanical trigger was designed so that data collection from the tool force system was synchronized with the video capture. A diagram of the custom built testing apparatus is shown below in Figure 2.2.

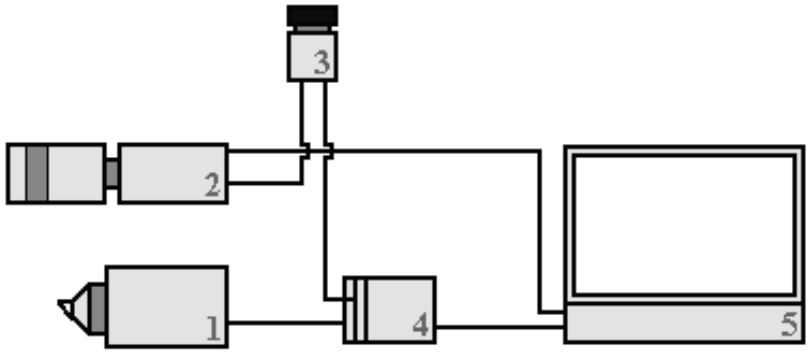

1. Tool Force Measurment System
2. InLine 500 - High Speed Camera
3. Mechanical Trigger - BNC to LAN
4. NI Data Acquisition System
5. Computer

Figure 2.2: High-frequency Tool Force/Camera System Set-Up

2.1.5. Cutting Tool Inserts. For all of the experiments, uncoated cobalt-bonded tungsten-carbide (WC-Co) sintered tool inserts were used. Tungsten-carbide was selected because of its wide use in GCI industrial machining and its better high-temperature wear characteristics for the cutting parameters selected. WC-Co was less susceptible to sudden failure by fracturing due to the interrupted/variable cutting

conditions, which are normally associated with near-surface machining. Finally, WC-Co is less expensive than ceramic or poly-crystalline diamond inserts. The inserts used with the low-frequency tool force system did not incorporate a chip breaker design on the rake face as this system was only used for experimental machining. The high-frequency tool force system used a Kennametal CNMG432 insert with a chip breaker in order to more accurately model industrial machining practices. For the cutting parameters selected and the WC-Co tool material the estimated wear mechanism was found to be on the boundary between onset of crater wear and the formation of build-up edge [7].

2.2. DESCRIPTION OF EXPERIMENTAL TESTING

2.2.1. Base Overview of Experiments. Each of the experiments performed followed similar machinability testing procedures, with only minimal changes in the casting production method, machining parameters, and tool force sampling rates used. All experiments used the AFS 5J or modified 5J test article produced from gray cast iron. Charge materials consisting of mixtures containing steel scrap, foundry returns, pig iron, and induction iron were either cupola or induction furnace melted. Alloy additions consisted of ferro-silicon (FeSi), ferro-manganese (FeMn), ferro-phosphorous (FeP), ferro-chrome (FeCr), ferro-sulfur (FeS), ferro-molybdenum (FeMo), copper, charge carbon (graphite), and SiC briquettes along with either Fe-Si-Sr (Superseed) or Fe-Si-Ca-Al (Vaxon) bearing inoculants. Castings were poured into green sand or resin-bonded sand molds and allowed to cool in the mold for roughly 30-45 minutes before shakeout. The castings were then shot-blasted before being pre-machined. Pre-machining was designed to remove draft angles around the circumferential regions only, the face of the castings were left unmachinined in order to evaluate the effects of the as-cast near-surface region.

Machinability testing was performed by locating each of the castings into the chuck of a HAAS computer numerically controlled (CNC) lathe. A surface map was generated in order to ensure the castings were installed properly without unnecessary

skew and to define the Z-axis offset (zero plane) for subsequent machining. Figure 2.3 illustrates the locations on the casting face used to define the plane from which a depth of cut could be specified. Four locations 1" (2.54 cm) apart measured at 90 degree intervals were averaged to determine the approximate position of the disk face.

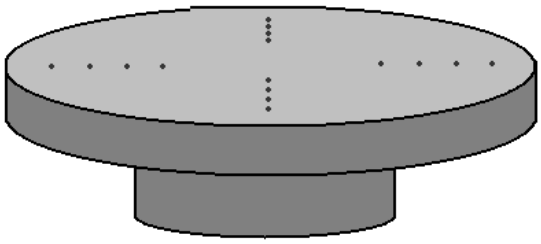

Figure 2.3: Locations Used to Determine Position of Casting Face (Z-axis Offset)

After calculating the zero plane the machinability testing was performed by using one of two specific facing operations (See Figure 2.4). The first operation was a simple facing cut with a constant depth of cut, feed rate, and cutting speed. Three-dimensional tool force data was collected over the entire duration of the cut as the cutting tool moved toward the center of the spinning casting. In some instances a high-speed camera was synchronized to the tool force measurement system to analyze chip formation. The second operation was a two-pass operation illustrated by Figure 2.4 (right). Due to the symmetry that occurs in the turning process only one radius of the disk is shown in the diagram (the casting center being located in the upper portion of the diagram). In the first pass the CNC tool is programmed to take a 0.105" (2.7 mm) DOC and cut for 1/3 of the casting radius, the DOC is then decreased to 0.070" (1.8 mm) cutting the next 1/3 radius, and the final DOC decreased to 0.035" (0.9 mm) cuts the final 1/3 radius. The second pass of the program follows in a similar manner only with the DOC step reversed (i.e. 0.035" to 0.105") such that after the second pass the casting surface is clean and a total of 0.140" (3.6 mm) has been removed from the casting face. By measuring the tool forces over the duration of both passes, it was possible to calculate the separate cutting forces associated with machining each 0.035" section in the near-surface region. This method

was developed because it allows the effects of as-cast surface dimensional variation to be eliminated after the first cut.

In addition to measuring the cutting forces, machine chips and cutting tool inserts were collected as an alternative method of evaluating machinability. The chips were collected from the same radial location (1/2 disk radius) for a 1 minute cutting time so that sampling conditions were kept constant. Chips were characterized by length and chip weight, as well as analysis under a scanning electron microscope (SEM). The chip morphology was used as an indication of the matrix microstructure behavior during the machining process. The cutting tools were cataloged and evaluated for tool wear using a NANOvea optical profilometer. The rake face, nose radius, and cutting edge feeding into the machined casting were given priority analysis. In addition to surface contour and wear a profile of the tool was generated to determine if build-up edge material adhered to the tool rake face.

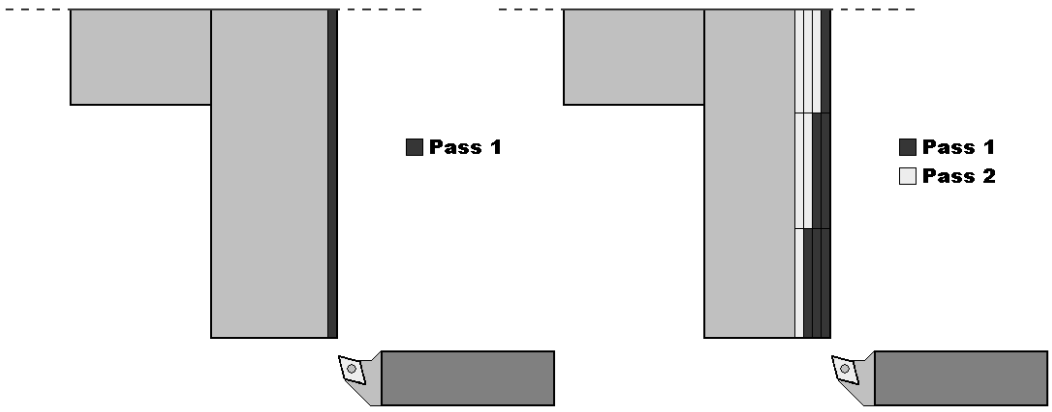

Figure 2.4: Comparison of Simple Facing (Left) to the DOC Program (Right)

Following machining, the 5J castings were tested for surface finish quality using a fixtured profilometer set-up, indented for brinell hardness, and then sectioned for quantitative metallography. The sectioned samples were mounted in bakelite, rough polished, and fine polished using diamond paste of 5um, 0.3um, and 0.05um particle sizes. All specimens were etched using a 2% nital (nitric acid + ethanol) solution in order

to distinguish between the ferrite and pearlite phases. The percentages of pearlite and ferrite along with graphite flake morphology were quantitatively evaluated using ImageJ analysis software. In each case the ferrite, pearlite, and graphite phases were selected by adjusting gray-scale thresholds in order to determine the area of each phases with respect to the overall area of the micrograph. Additional Vicker's microhardness indentions were made to distinguish between surface carbides and surface free-ferrite.

2.2.2. Near-Surface Microstructures and Graphite Morphology. Previous research has shown that graphite morphology and composition of alloying components can greatly affect cutting forces during machining. Carbon equivalent (CE) increases have been determined to cause a decrease in cutting forces by increasing the amount of graphite in the microstructure which in turn decreases the frictional forces between the tool and workpiece [39]. Increasing graphite flake length and reducing flake counts were also found to decrease tool wear and improve machinability during laboratory tests [40]. The distribution of ferrite, pearlite, and free carbides can influence the overall hardness of the microstructure which in turn will alter the machinability behavior. Microstructures containing mostly pearlite have been shown to machine much more efficiently than those consisting primarily of ferrite [41].

This experiment employed the use of cutting forces to determine the specific cutting energy (K) during the machining process. The specific cutting coefficient is a relationship between the main cutting force (F_c), feed rate (f), and the depth of cut (d) that allows the direct comparison of machinability results between various castings by removing the geometry dependence of the specific cutting energy equation. The specific cutting coefficient equation is given by Equation 4. By maintaining a constant feed rate and assuming proportionality between the cutting force and depth of cut it was possible to vary the depth of cut to examine how various depths from the cast surface would affect both the cutting force and the machinability. These results were then compared to the microstructure of the near-surface regions of the castings.

Standard gray iron AFS machinability test articles with varying CE values were cast in laboratory conditions. The laboratory castings were produced using a 100 lbs capacity basic magnesia-lined induction furnace to melt 80 lbs of high purity induction iron with alloy additions of Fe-75Si, FeS, Cu, FeCr, FeP, and charge carbon (graphite).

The melt was heated to a temperature of 2768 F (1520 C), de-slagged, and inoculated with Superseed at a temperature of 2715 F (1490 C) upon tapping into the pouring ladle. Both castings and chemistry samples were poured at a temperature of 2597 F (1425 C) into no-bake NovaSet bonded F70 silica sand molds. The castings were allowed to cool in-mold for approx 30 minutes prior to shake out and shot blast. After cleaning, de-gating, pre-machining, and installation into the CNC lathe, the TelC DKM2010 device was used to measure 3-dimensional cutting forces while the castings were machined using the DOC stepping program. In addition to the 0.035", 0.070", 0.105" DOC, the feed rate was 0.006"/rev with a cutting speed of 300 sfpm. From the cutting force, the specific cutting energy for each cut was calculated and plotted as a function of the distance from the as-cast surface. Quantitative metallography was used to evaluate the matrix microstructures and graphite flake morphologies. Distinctions were made between the as-cast surface and the underlying bulk material in an effort to quantify the difference between the near-surface region and body machining behavior.

2.2.3. Near-Surface Free-Ferrite. The relative percentages of the microconstituents (ferrite, pearlite, etc.) are of great importance, especially for high strength iron grades with low carbon equivalents (CE). This is because machinability has been found to decrease significantly with increasing strength due to the microstructures associated with higher strength irons [42]. Past research has shown that the machinability of gray iron castings is directly related to the microstructure and graphite morphology. Kahles and Field demonstrated that gray iron microstructure played a large role in machinability by comparing cutting speeds and tool lifetimes of both ferritic and pearlitic castings [40]. These findings suggested that 1) the low hardness of the irons containing a ferrite matrix microstructure produced less tool wear than those irons containing a pearlitic matrix microstructure and 2) the overall Brinell hardness of the iron reflected the presence of the softer graphite flakes, which was less than the actual hardness of matrix microstructure alone. This meant in certain cases where machining parameters were chosen based only on the Brinell hardness values of a casting, machinability would not necessarily be optimized and that the graphite was a significant contributor to casting machinability behavior. Later Voigt emphasized the characteristics of the near-surface region, including graphite flake morphology, as a major factor in determining

machinability. The characteristics of matrix microstructure and graphite flake morphologies were extensively studied by Voigt and Marwanga [10], who found that during the machining of gray iron the graphite flakes acted as crack initiators ahead of the advancing tool rake face. Also different graphite flake morphologies resulted in characteristically distinct decohesion and fracture in the "machining affected" (shear-compression) zone ahead and below the advancing tool. This experiment investigates how the cast surface geometry and microstructure including graphite-flake morphology and free-ferrite content impact the machinability of the near-surface region of gray iron castings. However, due to the numerous microstructural/machining variables it is often difficult to investigate one aspect of the near-surface microstructure solely with regard to machinability. As a result, a series of heat treatments were performed to decouple the variables of graphite flake morphology and matrix microstructure allowing simplified machinability determinations to be made.

Industrially cast standard gray iron AFS 5J machinability test articles were used to study the effect of matrix microstructure on near-surface machinability. 1000 lbs of cupola melted iron consisting of foundry returns and steel scrap charge materials with alloy additions of Fe-65Mo, Fe-75Mn, Cu, and SiC briquette were used to pour the test articles. The iron was tapped into a teapot pouring ladle at a temperature of 2700 F (1484 C) where it was in-ladle inoculated using 0.1% Superseed. The castings were poured at a temperature of 2630 F (1442 C) into Disamatic, Hunter, or Fisher produced green sand molds. The castings were allowed to cool in-mold for 30 minutes prior to shake out, shot-blasting, and de-gating.

Before machinability testing was performed the castings were separated into three groups: as-cast, normalized, and ferritized. Heat treatments were performed in order to alter the matrix microstructure of the test articles to produce primarily a pearlitic or ferritic microstructure. Pearlitic microstructures were produced by heating to 870 C, (1600F) soaking for one hour, and allowing the castings to air cool. Ferritic microstructures were produced by heating to 790 C (1450 F), soaking for 1 hour, and furnace cooling. The as-cast test articles were machinability tested immediately, while the heat treated articles underwent an additional pre-machining step. Using separation of variables and data collected from the as-cast articles a specified 0.015" (0.4 mm) DOC

was used to machine off the surface variations of the as-cast surface due to mold/metal interactions in the mold. This allowed only the effects of near-surface microstructure to impact the cutting forces (used to calculate specific cutting energy). Figure 2.5 presents an overview of the pre-machining operations performed on each group of castings.

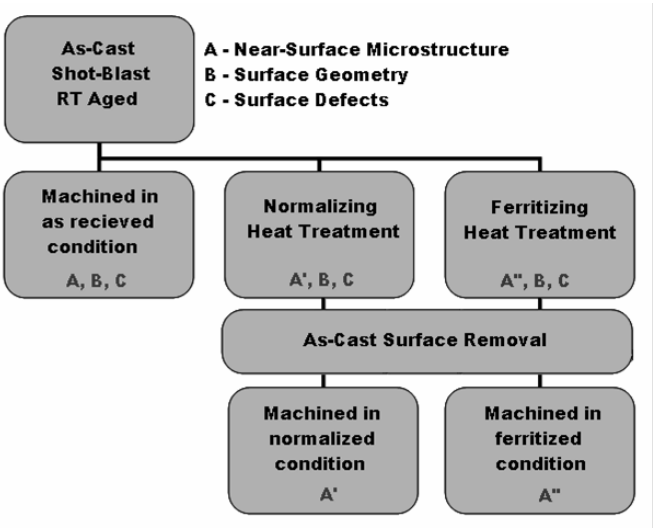

Figure 2.5: Matrix Microstructure Modification Experiment Flowchart

During machining and tool force data collection, machine chips were collected from each disk and later analyzed in a SEM. The DKM2010 tool force system and the custom-built high frequency tool force system synchronized with a high-frame rate camera were used in this experiment to capture cutting forces and machine chip formation characteristics simultaneously. After machining the castings were sectioned and quantitative metallography was performed in order to determine the extent of the matrix microstructure transformation.

2.2.4. Phosphorous and Chromium. In response to the AFS sponsored survey regarding machinability problems, modified gray iron AFS machinability test articles were produced from 95 pounds (lbs) of induction iron alloyed with Fe-75Si, Fe-65Mn, Cu, and charge carbon (graphite). The charge materials were melted in a laboratory 100lbs. basic (magnesia-lined) induction furnace and heated to a temperature of 2768 F

(1520 C) and de-slagged. Prior to tapping alloy additions of Fe-26.6P and Fe-50Cr were immersed and stirred into the melt. The iron was tapped at 2715 F (1490 C) into a pouring ladle where it was inoculated in-ladle using 0.7 lbs of Vaxon D (a Ca bearing Fe-Si designed to reduce chilling, refine eutectic cell size, and increase content of type A graphite). The castings were poured at a temperature of 2625 F (1440 C) into no-bake NovaSet bonded F70 silica sand molds and after 30 minutes were shaken out. The castings were then de-gated, shot-blast, and pre-machined to remove only the draft. Cutting forces were measured using the DKM2010 system and a series of 6 sequential simple facing cuts were performed. The machining parameters consisted of a 0.015" DOC, a 0.006 "/rev feed rate, and a cutting speed of 300 sfpm. Sectioning of the castings was performed to obtain samples for quantitative metallography and chemistry (shown below in Table 2.1). Samples were etched with stead's reagent in addition to 2% nital in order to resolve the eutectic cells and the presence of steadite. Additionally thermodynamic modeling was performed to describe the effects of stable iron-phosphorous-graphite and metastable iron-chromium-phosphide-carbide formation on machining behavior.

Table 2.1: Compositions for Unalloyed, P-alloyed, and P+Cr-Alloyed Castings (Wt %)

Casting	C	Si	P	Cr	S	Mn	Cu	Al	Ti
Unalloyed	3.23	2.454	0.013	0.014	0.012	0.393	0.254	0.003	0.042
P-alloyed	3.34	2.483	0.096	0.042	0.015	0.391	0.262	0.004	0.042
P+Cr-alloyed	3.29	2.456	0.115	0.379	0.015	0.397	0.260	0.004	0.046

2.3. DESCRIPTION OF CASE STUDY

Automotive brake rotor castings (shown below) produced at a foundry experienced an 88% decrease in tool life when produced on a newly installed automatic molding line. Three sets of castings were received for machinability analysis. The three sets of class 35 GCI brake rotors were produced from induction melted steel scrap and foundry returns. To produce the castings 1450 lbs (600 kg) of molten iron were tapped

from the induction furnace at a temperature of 2590 F (1420 C) and inoculated with Fe-75Si before pouring the green sand molds at 2535 F (1390 C). Two sets represented castings from the old and new molding lines. One set contained castings with an alloy addition of antimony (Sb) in an effort to stabilize pearlite produced on a Fisher green sand line, thereby improving machinability.

The castings were first tested for brinell hardness and surface roughness prior to being chucked into a CNC lathe. The reduced surface area of the castings decreased the number of measurements per radius for the Z-axis offset, so additional measurements were made every 45^{o} rather than every 90^{o}. The geometry of the castings was similar to that of the AFS 5J machinability article (Figure 2.6), and as a result a similar procedure was used to evaluate machinability. The DOC stepping program was not used due to the shallow depth of cut used by the foundry's machine shop (< 0.035"), therefore only the cutting forces measured by the DKM2010 system over the duration of a simple facing cut were considered. Following machining, the castings were sectioned for quantitative metallography samples and tested using Vicker's microhardness.

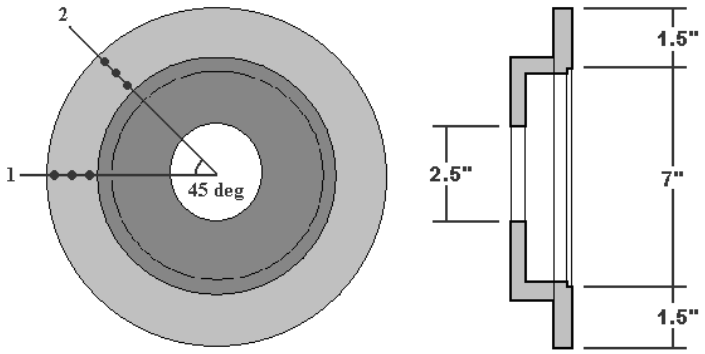

Figure 2.6: Dimensions and Measurement Locations of Brake Rotor Casting

3. NEAR-SURFACE MICROSTRUCTURES AND GRAPHITE MORPHOLOGY

3.1. RESULTS OF LABORATORY PRODUCED CASTINGS

3.1.1. Machinability Results. The two pass multiple DOC stepping program was used to measure the main cutting forces as a function of depth from the as-cast surface of AFS machinability test articles cast from separate heats. A sample of the collected tool force data from one complete DOC stepping program performed is shown below in Figure 3.1. As expected, Step 1 (DOC = 0.105") of Pass 1 exhibited a much larger cutting force than Step 3 (0.035") of Pass 1. It is interesting to compare the change in slope of the measured cutting forces from Pass 1 to Pass 2. The variation from Pass 1 to Pass 2 was the result of variations of the near-surface microstructures due to chemical interactions and diffusion with the mold materials during solidification. In Pass 2, the inconsistencies of the as-cast surface have been removed and the measured cutting forces stabilized.

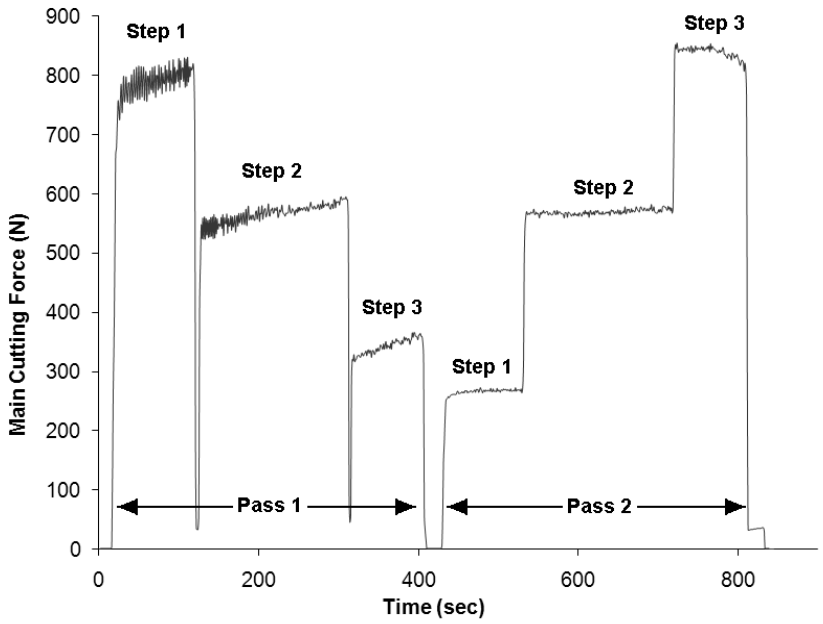

Figure 3.1: Example of Data Collected During Passes 1 and 2 from the Cast Surface

The specific cutting energy, K (kN/mm^2), was calculated for each separate layer using Equation 4 and plotted versus depth of cut. An example of the results obtained from machining one test article is given below in Figure 3.2. During Pass 1, larger values of K were obtained for the casting surface (Step 3) than for the second and third layers (Steps 2 and 1, respectively). The left portion of the plot showed some variations in the measured main cutting force as a result of differences in the depth of cut (surface variations) near the cast surface. The right part of this plot contains information obtained from the same machining procedure in the central region of the casting body. Cuts made within the casting body had less variation in the K value because a more stable depth of cut and matrix microstructure was obtained during cutting.

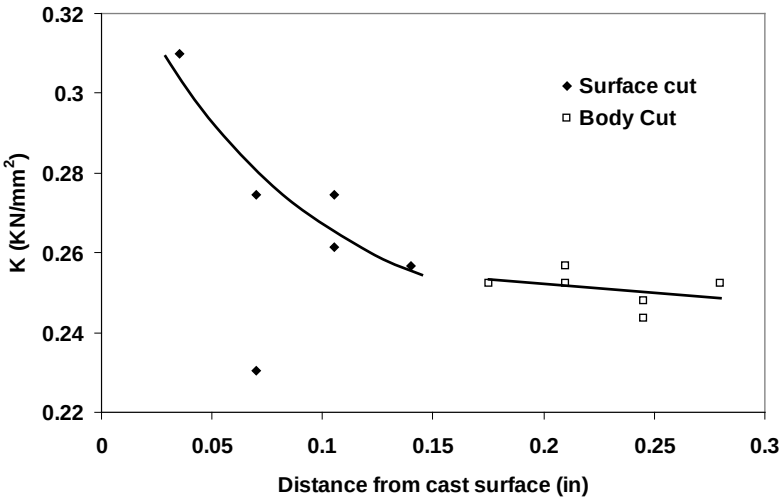

Figure 3.2: Specific Cutting Energy as a Function of Distance Beneath Cast Surface

Drawing upon references in the literature it was thought that carbon equivalent (CE) values would provide a relative measure of the near-surface microstructures present in each of the test articles. For example the test articles with greater CE values were expected to contain higher percentages of free-ferrite near the as-cast surface than test articles with lower CE values. The effects of the near-surface microstructures would then be evident in the collected tool force and specific cutting energy data. Figure 3.3 depicts

a plot of the specific cutting energy as a function of distance from the as-cast surface for each of the five test articles organized by carbon equivalent. From Figure 3.3A it was initially determined that a correlation between CE value and specific cutting energy was unlikely. The specific cutting energy differences between two 3.95 CE heats was found to be just as great as differences between one 3.95 and 4.23 CE heat. However, after dividing the data into hypo-eutectic and hyper-eutectic data sets in Figure 3.3B, it was found that a slight correlation may exist. Regardless of the viewpoint taken regarding CE versus specific cutting energy, the data sets from both figures confirmed a strong dependence of specific cutting energy on distance from the as-cast surface. This data suggested that a more complex microstructural dependence existed. Quantitative metallography was used to further investigate and determine the effects of near-surface microstructure on the specific cutting energy behavior.

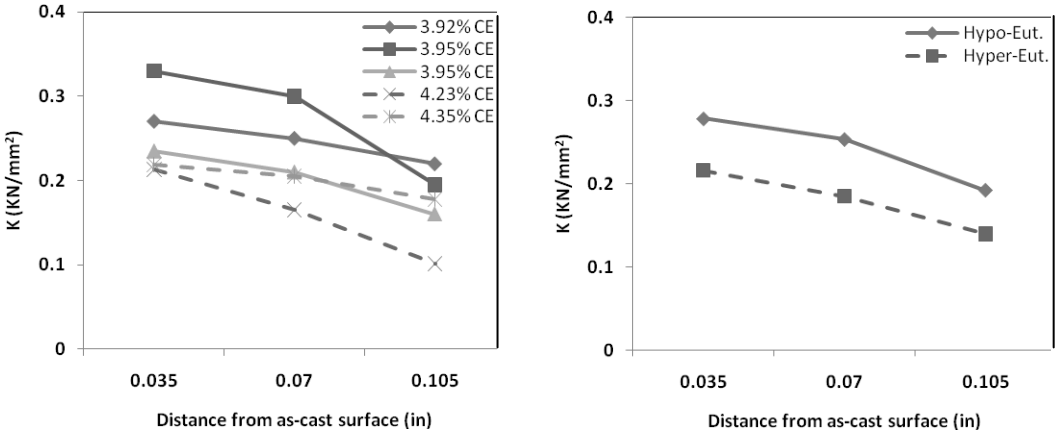

A) B)

Figure 3.3: Influence of Position of Cutting Layer on Cutting Forces (Lab Castings)

3.1.2. Metallographic Results. Quantitative metallographic examination of the laboratory produced test articles indicated a wide range of free-ferrite and pearlite microconstituents as well as graphite flake lengths. These microstructural differences were found to be the result of slight variations in the tap/pouring temperatures, resin-

bonded sand mold chemistry, shakeout times, and charge metal chemistry between heats. Table 3.1 below shows a summary of the chemical composition range between the different test articles.

Table 3.1: Range of Chemical Compositions for Laboratory Castings (Weight %)

CE	C	Si	S	Mn	Cr	P	Cu	Al	Ti	B
3.89	3.25	1.93	0.04	0.37	0.08	0.05	0.33	0.001	0.002	0.004
4.33	3.44	2.00	0.06	0.53	0.11	0.06	0.40	0.004	0.003	0.015

Metallurgically it was found that the test articles exhibiting the greatest specific cutting energies and cutting forces, were those with the greatest percentage of free-ferrite in the near-surface microstructures. In every case the greatest percentage of free-ferrite was found within the first 0.035" of the as-cast surface and thus was determined to be a significant factor for the influence of cutting layer on cutting force in Figure 3.3. Table 3.2 and Figure 3.4 below offer a summary of the metallurgical data collected regarding ferrite/pearlite percentages, graphite flake lengths, and the measured cutting forces as a function of distance from the as-cast surface. Initially it was thought that a dependence on carbon equivalent was solely responsible for differences in near-surface ferrite percentages, but the idea was rejected due to the fact that the production variables from heat to heat were not held constant.

From Figure 3.4 it is interesting to note that the percentage of free-ferrite is greatest near the as-cast surface and conversely the percentage of pearlite increases as distances from the as-cast surface increase. The graphite flake lengths can also be seen to increase, while the cutting forces decrease with increasing distances from the as-cast surface. The table further supports that the assumption of free-ferrite content estimated by carbon equivalent is incorrect. The data does suggest that increased free-ferrite contents may be responsible for elevated cutting forces, however the graphite flake length behavior can also be seen to be a factor. The remainder of this experiment focuses on the effects of graphite flake morphology on machinability, while the next section deals with free-ferrite and the matrix microstructure effects.

Table 3.2: Summary of Quantitative Metallography and Tool Force Data

%CE	Distance from AC Surface (in.)	%Ferrite	%Pearlite	Flake Length (um)	Cutting Force (N)
3.92	0.035	35.1	44.9	48.0	345
	0.070	1.4	76.2	53.0	223
	0.105	1.8	78.3	48.0	225
3.95	0.035	37.6	41.5	52.1	487
	0.070	7.8	68.2	56.5	218
	0.105	2.2	76.8	67.8	155
3.95	0.035	37	48.5	51.0	263
	0.070	2.4	83.4	51.0	220
	0.105	0.7	85.4	53.0	155
4.12	0.035	33.9	50.1	51.0	216
	0.070	24.4	61.3	58.0	206
	0.105	3.8	82.7	62.0	156
4.23	0.035	45.2	39.7	64.5	267
	0.070	37.3	29.3	69.9	130
	0.105	26.9	52.3	71.2	101

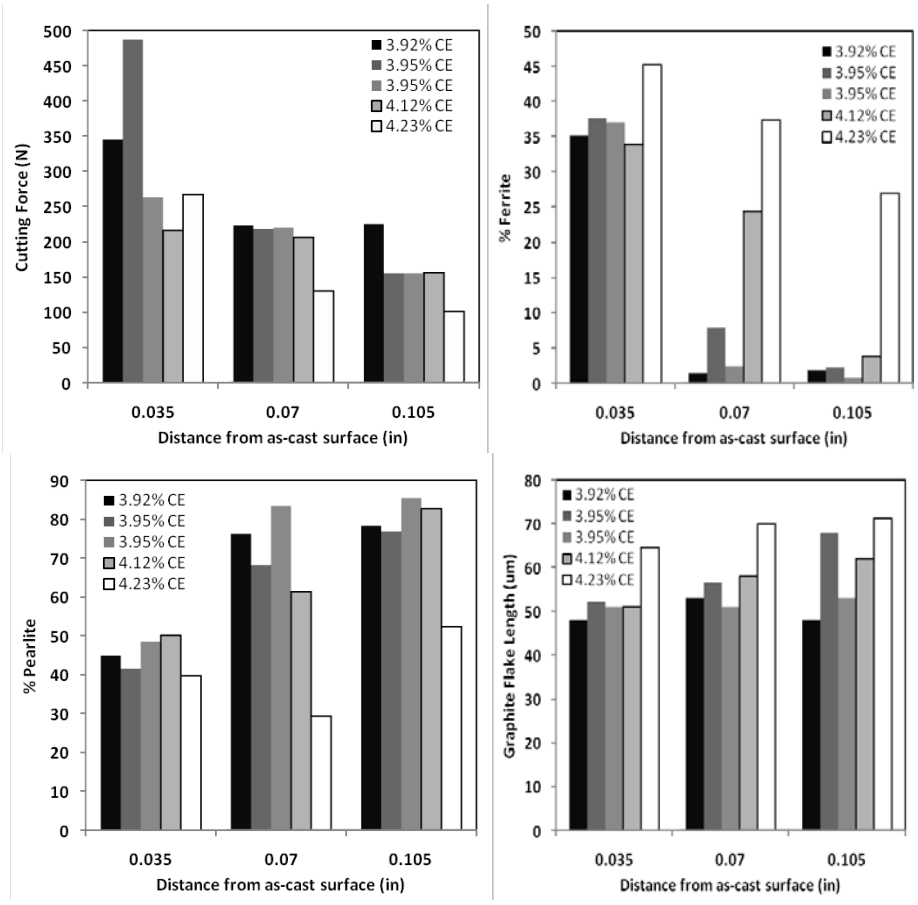

Figure 3.4: Plot of Quantitative Metallography and Tool Force Data

3.2. EFFECTS OF GRAPHITE FLAKE MORPHOLOGY AND LENGTH

The main cutting force values measured at the cast surface and the associated tool wear rates depended on many factors, some of which included machining parameters, surface geometry (tolerance, roughness), surface/subsurface defects, and microstructure of the cast surface. In this study, the experimental data was analyzed only from the position of cast surface metallurgy.

Solidification time and cooling rate are two of the major parameters influencing the cast iron microstructure. From the cutting force data collected, the cast surface of the test articles required approximately 30-50% larger specific cutting energies during the machining process. One possible explanation for the differences between the cutting forces of the cast surface and internal microstructures was based on variations in solidification parameters in these two regions. Solidification processes near the cast surface region and in the casting body were evaluated using MAGMASOFT casting software. The solidification time of the casting body was calculated to be 40 -50 % longer than the cast surface, shown below in Figure 3.5.

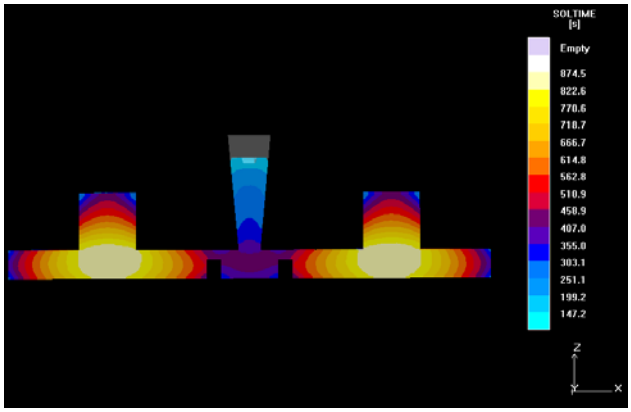

Figure 3.5: Solidification Rate Data from MAGMASOFT Simulation

These iron solidification rates were responsible for the primary differences in solidification structure as well as secondary austenite/ferrite-pearlite transformation during the eutectoid reaction. Another possible explanation deals with shakeout time and

casting duration within the mold. The longer the test articles remained in the mold, the greater the chance of secondary graphitization to occur at the as-cast surface as the microstructure temperatures cooled through the eutectoid transformation range [31, 32]. Sample microstructures of the near-surface region and casting body for different free-ferrite percentages are given in Figure 3.6. The quantitative evaluation of graphite size is given in Figure 3.7. Two methods were used for the calculation of graphite length. The first used the maximum graphite length and the second, the Feret's (circumscribed) diameter for the 20 longest particles. The first method gave results more sensitive to sample location. Surface layers were found to exhibit significantly shorter graphite flake lengths when compared to the central region of the castings.

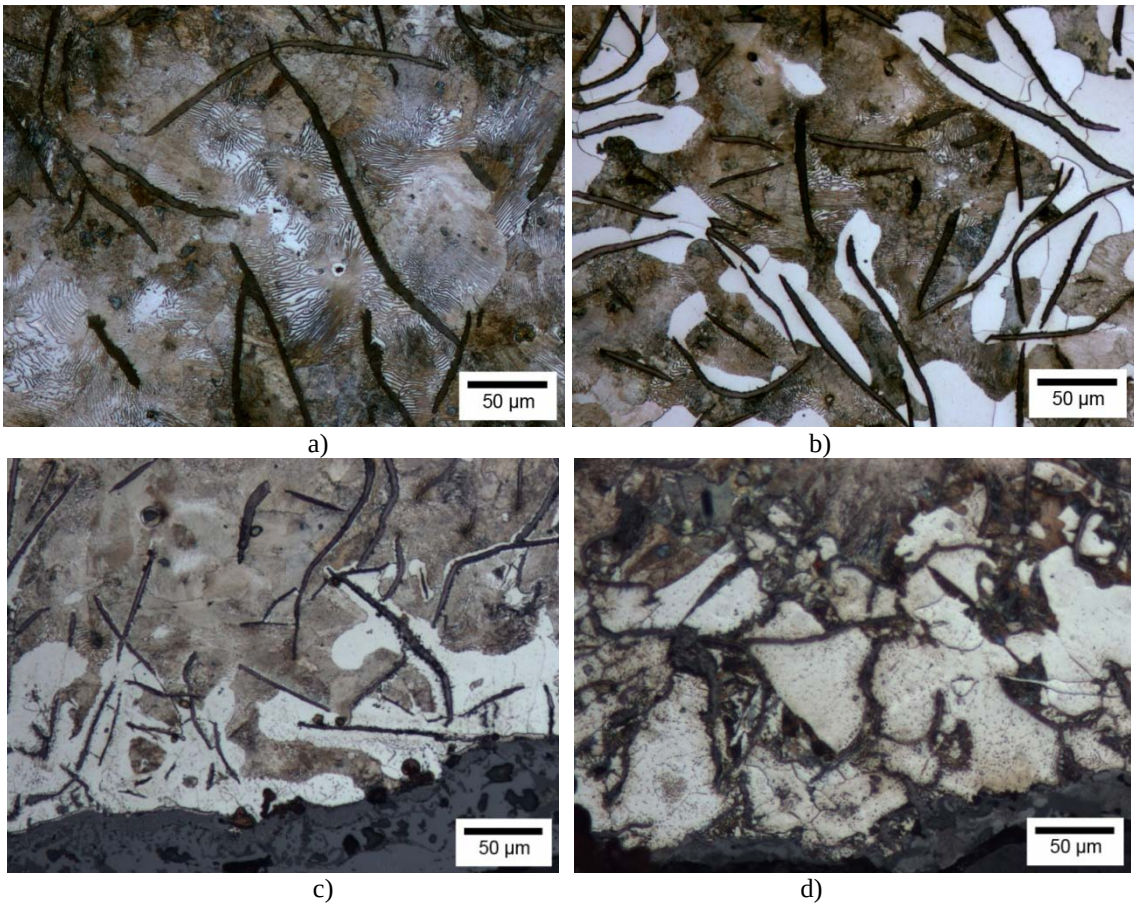

a) b)

c) d)

Figure 3.6: Microstructure of Test Articles with Low and High Ferrite Percentages. a) Low Ferrite Body, b) High Ferrite Body, c) Low Ferrite Cast Surface, d) High Ferrite Cast surface

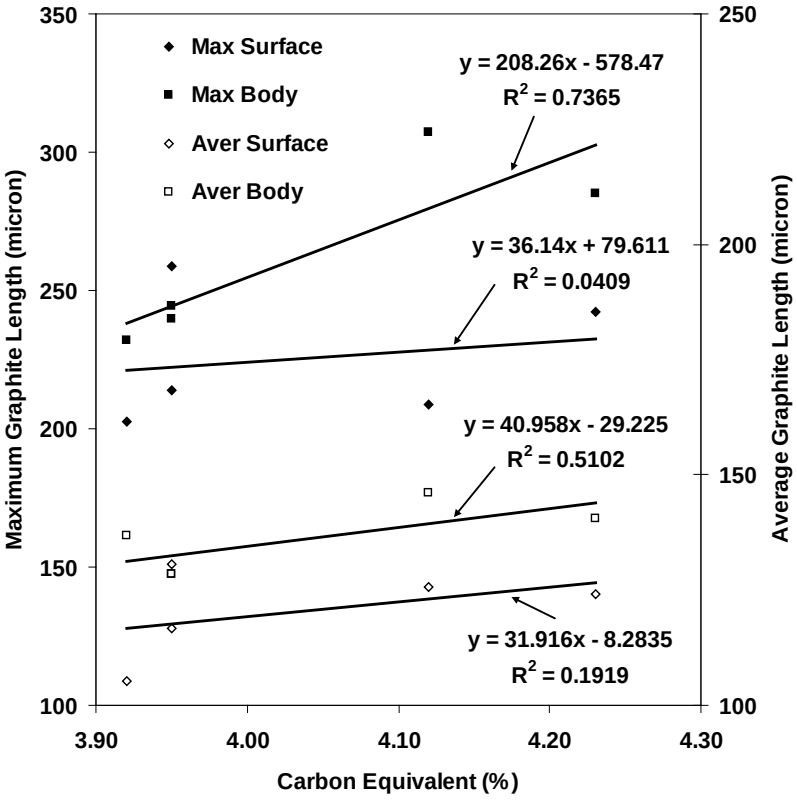

Figure 3.7: Graphite Size in Different Locations with Respect to Variations in CE

For the volume of graphite phase in different parts of the casting, the primary eutectic structure with the smallest graphite flake size provided the shortest average distance (S) between neighboring graphite particles. An example of the distribution of graphite flake neighboring distance for the surface and casting body is given in Figure 3.8. Table 3.4 illustrates an example of all statistical graphite parameters for surface layer and casting body for the same casting with carbon equivalent 4.23%. Notice that the surface and body had the similar areas (volume) of graphite (12-13%) while lengths and number of particles were significantly different. The sum of these changes impacted the graphite flake neighboring distance.

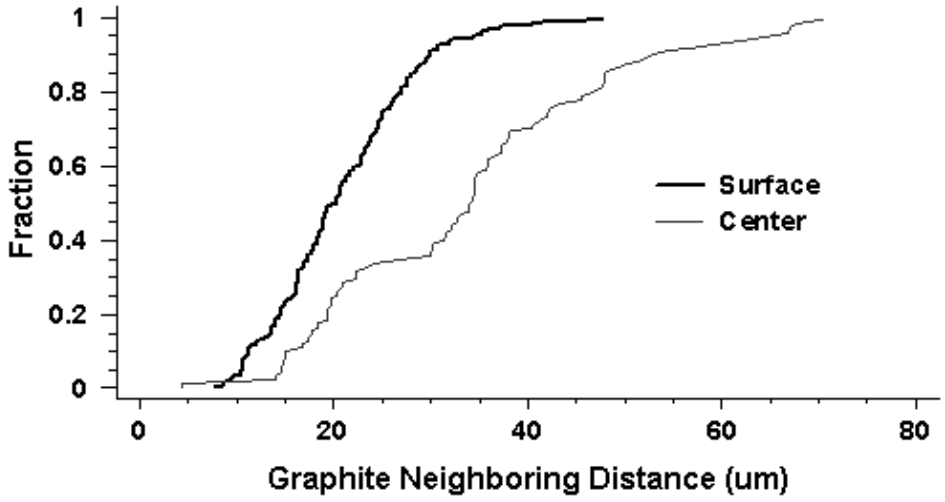

Figure 3.8: Graphite Flake Neighboring Distance Distribution for the Surface and Casting Body in a Casting with 4.23% CE

Table 3.4. Example of Quantitative Analysis of Flake Graphite in Surface Layer and Casting Body (4.23% CE)

Position	**Area, %**	**Max. Length, µm**	**Feret's Dia., µm**	**Particles, number/m^2**	**Total Perimeter, µm/mm^2**	**Avg. Neighboring Distance, µm**
Surface	13	150	106	803	77140	26.5
Body	12	284	140	270	40608	33.4

Both the carbon diffusion distance and diffusion time have an influence on the ferrite/pearlite transformation of undercooled austenite. Carbon is required to travel shorter diffusion distances in surface regions which can be seen in Figure 3.8, due to the higher percentage of types D and E graphite. Directly competing with the shorter diffusion distance is both a higher cooling rate and shorter transformation time when compared to the casting body. At first approximation, the summary effects of these factors could be evaluated using the relationship between diffusion coefficient of carbon through the matrix (D), diffusion distance (S), and diffusion time (τ):

$$S \cong \sqrt{D\tau} \tag{11}$$

It is important to mention that doubling the diffusion distance (S) increases the transformation time (τ) by a multiple of four. Therefore, changes in graphite distribution can have a great effect on the formation of free-ferrite in the near-surface region. At the surface of a casting when solidification occurs rapidly there may not be sufficient time to for optimum nucleation of graphite. This results in higher counts of shorter graphite flakes and large regions of free-ferrite, as carbon diffuses toward nearby graphite flakes during in-mold cooling. The formation of this free-ferrite as a result of diffusion can be further reduced by ensuring the proper mold material composition to reduce reactions with the melt and ensuring the castings are shaken out near-above the eutectoid temperature to increase the cooling rate, thereby enhancing the percentage of pearlite formed.

3.3. EFFECTS OF MATERIAL BUILD-UP ON CUTTING TOOLS

Many parameters were to influence the cutting force/specific cutting energy of the near-surface region, including the matrix microstructure and the graphite flake morphology. However, the near-surface microstructures can also alter the mechanisms of the machining process. When the tip of the tool enters into the heterogeneous iron matrix, the cutting force rises due to alloy micro-deformation. The energy spent on elastic and plastic micro-deformation depends on the microstructure of the iron as well as the volume of the region deformed. However, the volume of the deformed region also depends on the tool tip geometry. Moreover, the tool tip geometry is not a constant parameter and can be changed as a result of tool wear or build-up of cutting material on the tool surface. Both the ferrite volume and graphite size/distribution have an influence on cutting force. In particular, the micro-volumes of ferrite phase enclosed between the brittle and weak graphite phase could increase the energy of plastic deformation by enlarging the deformation region before the chip detaches by fracture. From this

perspective, size and graphite particle distributions are important. If graphite particles are small, for example, interdendritic D-type, significant plastic deformation of ferrite can occur without chips breaking. When ferrite is enclosed between larger size graphite flakes, the weak phase initiates the chip breaking process. The possible build up of ferrite on the tool surface, which is illustrated in Figure 3.9, increases the volume of the compression region and required deformation and fracture energy.

In Figure 3.9, Cut 1 refers to a single 0.035" DOC facing operation of the as-cast surface, while Cuts 2 and 3 were made sequentially using the same DOC as Cut 1. It can be seen that as the near-surface region is removed (or the distance from the as-cast surface increases) the amount of build-up edge material adhering to the tool face was decreased, as well as the associated tool wear. Due to the high percentages of free-ferrite found in the near-surface regions the material build-up behavior was attributed to free-ferrite. For this reason the next section details the effects of free-ferrite in the near-surface microstructure and its specific effects on the chip formation process.

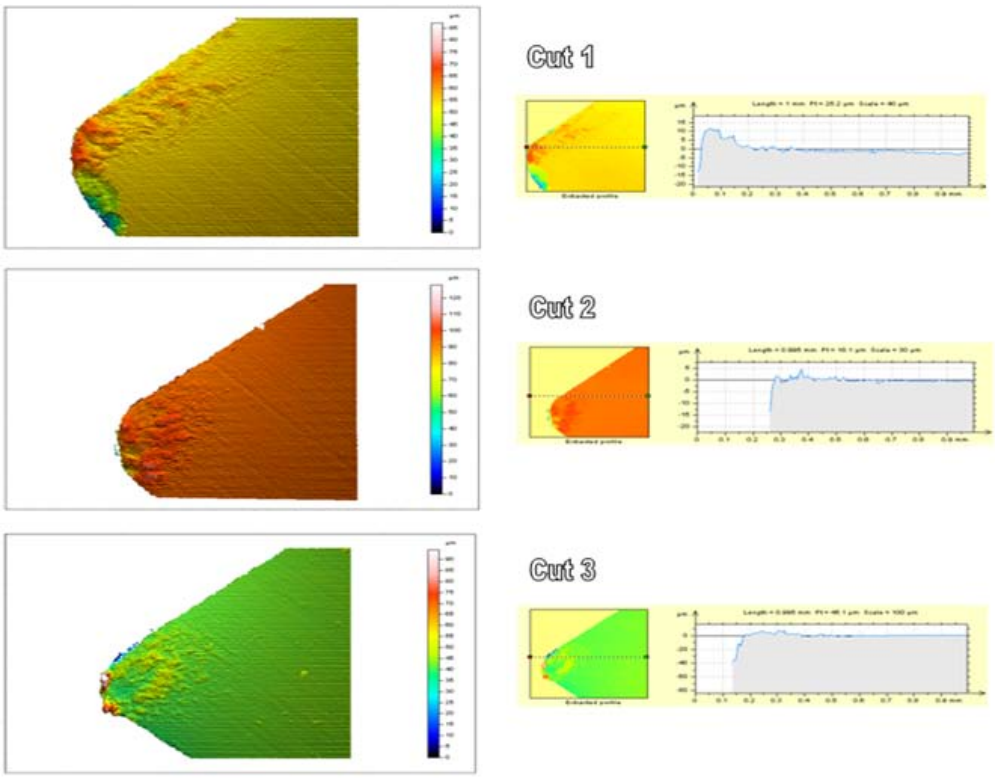

Figure 3.9: Build-Up of Material on Tip of the Cutting Tool

4. NEAR-SURFACE FREE-FERRITE

4.1. DIFFERENCE IN SURFACE AND BODY CUTTING FORCES

Initial machinability testing of untreated Class 40 AFS test articles illustrated the combined effect of surface geometry, graphite morphology, and free-ferrite in the near-surface region. Z-axis offset (zero plane) data indicated that the maximum height variation of as-cast surface was 0.030" and the surface elevation was heavily dependent on radial location. Figures 4.1 and 4.2 present the variations in the average specific cutting energy (K) during machining of the as-cast surface and subsequent body layers. The as-cast surface showed significantly larger specific cutting energies than the following body layers. This effect took place within the first 0.015" of the as-cast surface. In some cases the specific cutting energy of the second body layer (0.015"-0.030") showed a minimum value which then rose slightly as the distance beneath the as-cast surface increased. The combined effects of surface geometry, ferrite content, and graphite morphology was determined to be responsible for the large differences in the specific cutting energy in the near-surface region.

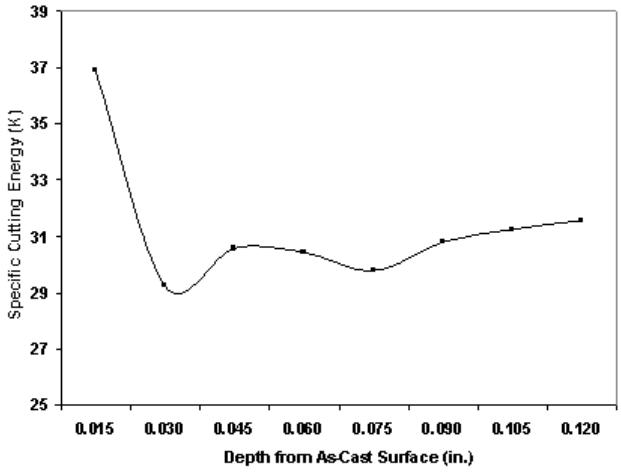

Figure 4.1: Average Specific Cutting Energy (K) Versus Position of Cutting Surface (from As-Cast Surface to Casting Body)

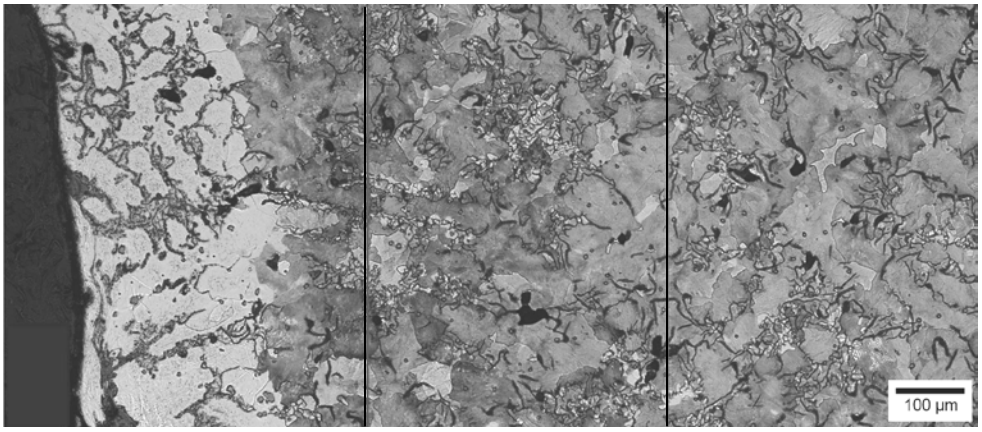

Figure 4.2: Near-Surface Microstructure as a Function of Depth into Casting Interior

A second test on the as-cast Class 40 castings was performed using synchronized high speed devices (tool force dynamometer and high-speed video camera). In this test the depth of cut was increased to 0.030” and cutting speed was decreased to 50 sfpm. Cutting speed was limited by video camera capture rate. The as-cast surface cutting force showed a higher mean value and larger variations over the duration of the facing cut (Figure 4.3). The use of the high frequency DAQ allowed for the evaluation of cutting force fluctuations in greater detail (Figure 4.4). In both figures, the possible variation of cutting force due to noise (+/- 4 N) is shown by the shaded area. It could be seen that the force variations during the surface cut were significantly larger than those of the body cut. These greater variations were attributed to both the surface topology and complexity of near-surface microstructure. STATGRAPHICS statistical analysis of cutting forces was performed in order to determine an average value, standard variations, as well as the departure from normal probability (See Table 4.1). In general, data will approximate a normal probability distribution if only a single variable is acting. According to statistical t-tests, the two cutting force data sets had a 99% probability of being significantly different. The average tool forces for surface and body cuts were 383.8 N and 319.0 N, respectively (Figure 4.5). The standard deviation of surface cutting was also found to be 3 times larger than that of the body cut (Table 4.1).

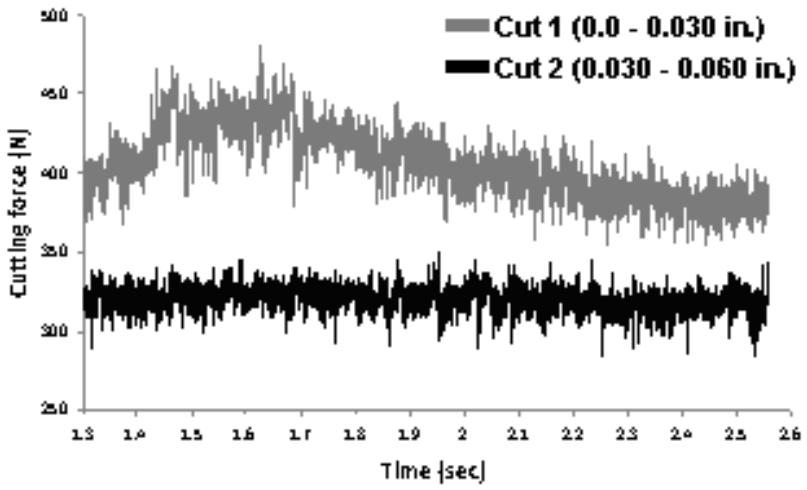

Figure 4.3: Cutting Force Variation for Surface and Body Cut of Untreated Iron

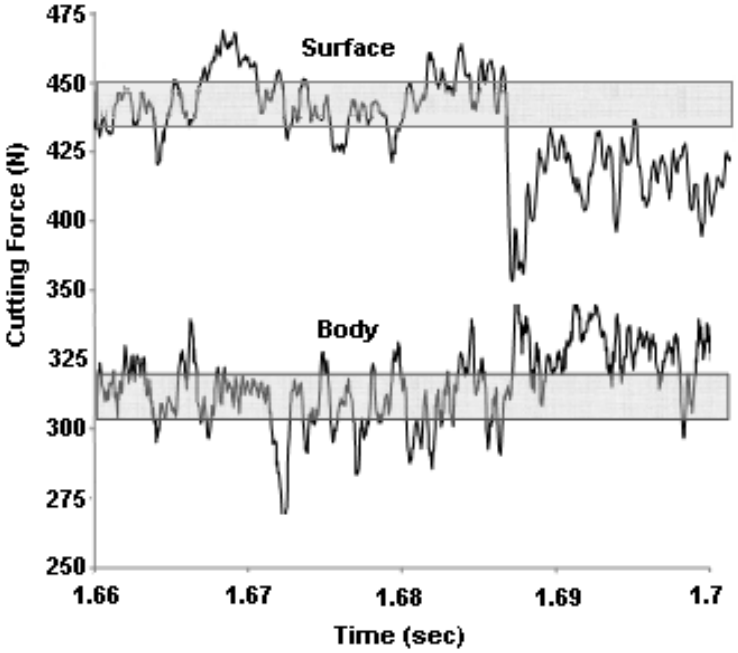

Figure 4.4: High Frequency Plots Comparing Surface and Body Cutting Forces

Table 4.1: Untreated Test Article Statistics Summary of Surface and Body Cuts

Cut #	Cutting Depth	Count	Avg. Fc (N)	Std Dev.	Min. Fc	Max. Fc
1	0-0.030”	160000	383.8	63.3	304	480.3
2	0.030-0.060”	160000	319	24.5	262	351.1

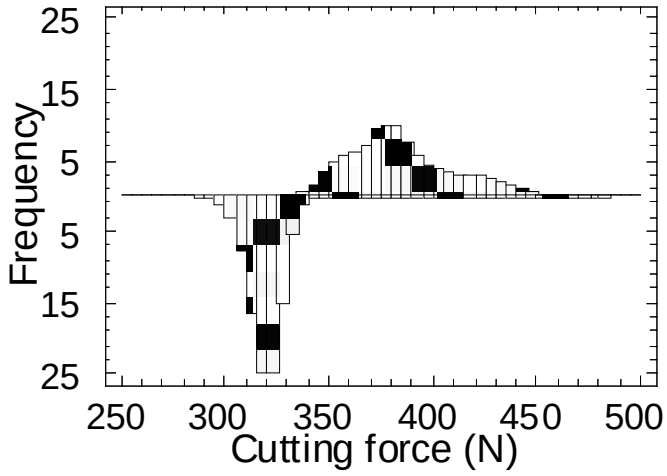

Figure 4.5: Histogram of Cutting Forces for Surface Cut (top) and Body Cut (Bottom)

In Figure 4.6 the surface cutting forces had significant departures from a normal distribution in both the upper and lower force regions, indicating that more than two variables were acting. These multiple variables were attributed to graphite morphology, ferrite content, and surface geometry. In order to better understand the possible effects of these variables, a model experiment was performed using heat treated castings. In this experiment the matrix variable was specifically investigated separately from graphite flake morphology and cast surface topology.

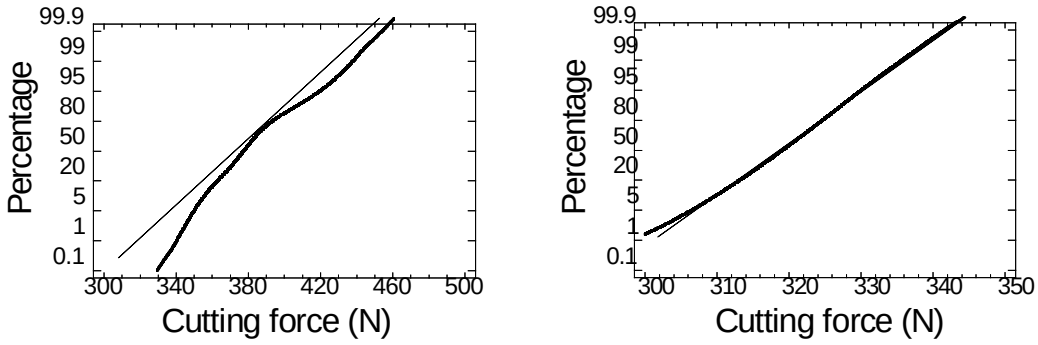

Figure 4.6: Normal Probability Plots for Surface Cut (left) and Body Cut (right)

4.2. MACHINABILITY OF FERRITIC AND PEARLITIC IRONS

Heat treated iron castings were rough machined to remove surface geometry effects. It is important to note that after rough machining the variation in the measured cutting forces during the cutting process was still larger than the +/- 4N noise level for both heat treatment conditions. These variations were the result of the chip forming process.

Figure 4.7 shows the comparison of the cutting tool forces between the pearlitic and ferritized test articles along with the areas of tool force electronic noise. The data in the figure confirms the fact that irons with higher percentages of pearlite in the matrix microstructure require more energy to machine when using the same machining parameters. It is important to note that the variation in the measured cutting tool forces of the ferritic iron was greater than that of the pearlitic iron. Analysis of the graphite flake morphology indicated that both test articles contained primarily type A graphite with a maximum flake length of 36 microns (Size 2). This behavior of cutting force confirmed the hypothesis that the matrix microstructure surrounding the graphite flakes played a significant role on both the magnitude and variation of the tool force during machining.

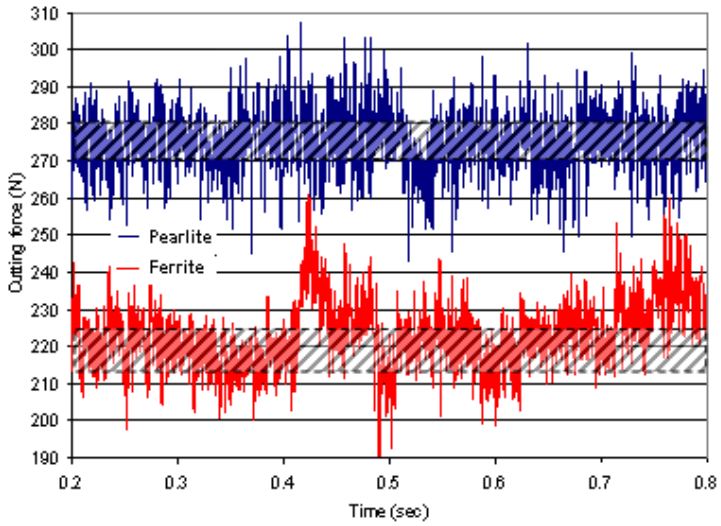

Figure 4.7: Variations of Cutting Forces for Pearlitic and Ferritic Irons

Results from a statistical evaluation of cutting tool forces from both pearlitic and ferritized test articles are shown in Figure 4.8. In this study 100,000 measured tool force data points were compared using statistical software. Figure 4.8 shows that these two sets of data had different types of departure from normal probability. The pearlitic iron showed a departure from normal distribution at low cutting force values while the ferritic iron showed a departure from normal distribution at high cutting force values. The causes of these different departures from the normal probability plot were analyzed together with chip formation data from high-speed video.

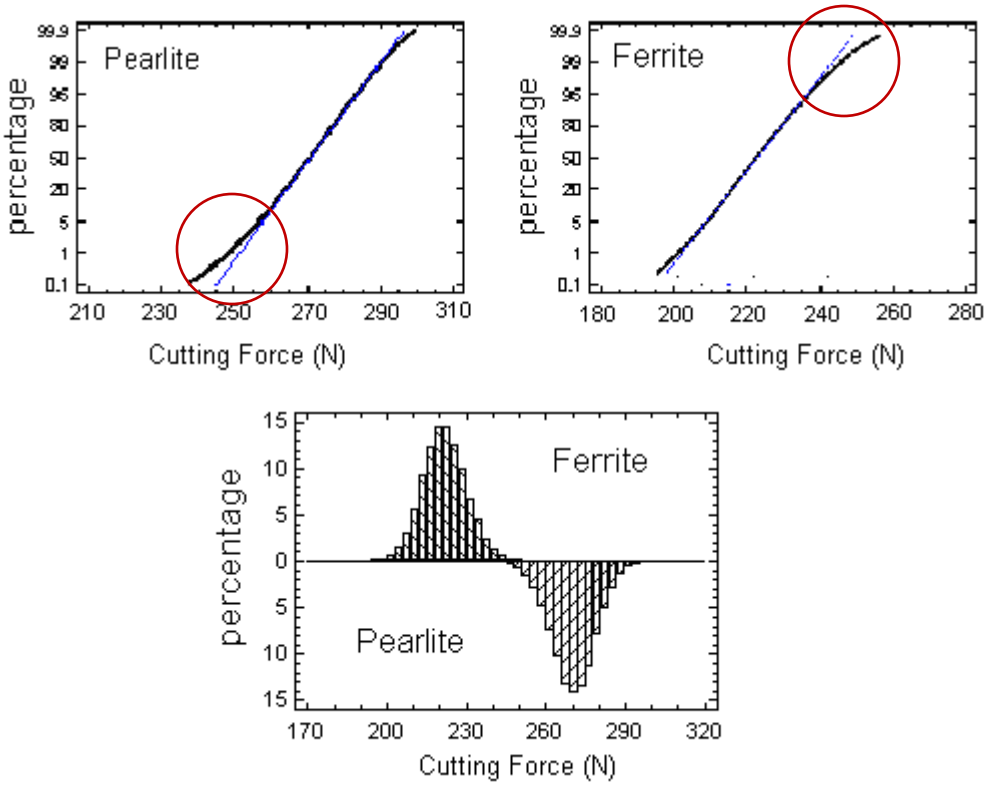

Figure 4.8: Statistical Analysis of Cutting Force for Pearlitic and Ferritic Irons

4.3. VIDEO ANALYSIS OF CUTTING PROCESS

The machining process of the heat treated irons was additionally analyzed using a high speed video camera synchronized with a tool force measurement system. Images

captured from the high-speed video camera were analyzed frame by frame and compared to the main cutting force value measured at the same moment. Figure 4.9 shows an example of the cyclic maximum and minimum peaks in the measured cutting tool force measured during the video analysis of the pearlitic iron. These peaks can be attributed to three major phenomena depending on the magnitude and direction. The maximum peaks were found to occur when wide/thick chips began to form and curl more than one rotation. The small minimum peaks were categorized as shear step discontinuity (partial crack) formations, while the larger minimum peaks were associated with chip break-off events. Thus the chip behavior appeared to be similar to classical discontinuous chip formation in which shear steps form partial cracks that do not lead to complete rupture and where complete chip break-off events occurred less frequently.

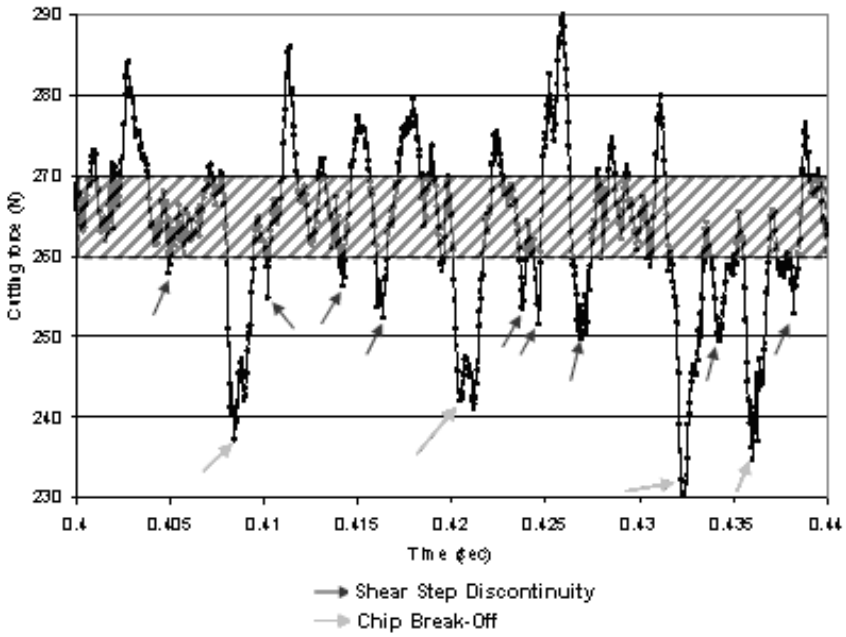

Figure 4.9: Variation of Cutting Forces During Chip Formation for Pearlitic Cast Iron

Similar analysis of the ferritic iron test articles found significant differences in the chip formation behavior from that of the pearlitic iron test articles. Both the high-speed camera and cutting tool force data indicated a fewer number of minimum peaks occurring

over the same machining time. Chip break-off events were also found to occur at less frequent intervals, suggesting that longer chips were formed in the ferritic test articles (Figure 4.10). In Figure 4.10 over the same machining time interval, five major chip break-off events occurred for the pearlitic test articles, while only one occurred for the ferritic test articles. In Figure 4.11, a smaller machining time interval was investigated and again it was found that a higher frequency of shear step discontinuity (partial cracks) events occurred than chip break-off events. At the same time, ferritic iron had a larger amount of fluctuations above an average level. These fluctuations periodically became so large that the cutting force equaled the average cutting force for pearlitic iron (Figure 4.7). An additional analysis of still photos from the high speed video data showed that build-up of machined material along the tool edge took place at these moments. From previous work the presence of unstable build-up edge can result in poor surface finish caused by material break-off adhered to the newly machined surface, as well as a decrease in cutting tool lifetime. Conversely stable build-up edge can result in a protective layer forming on the leading edge (rake face) of the tool that protects the tool from abrasion wear.

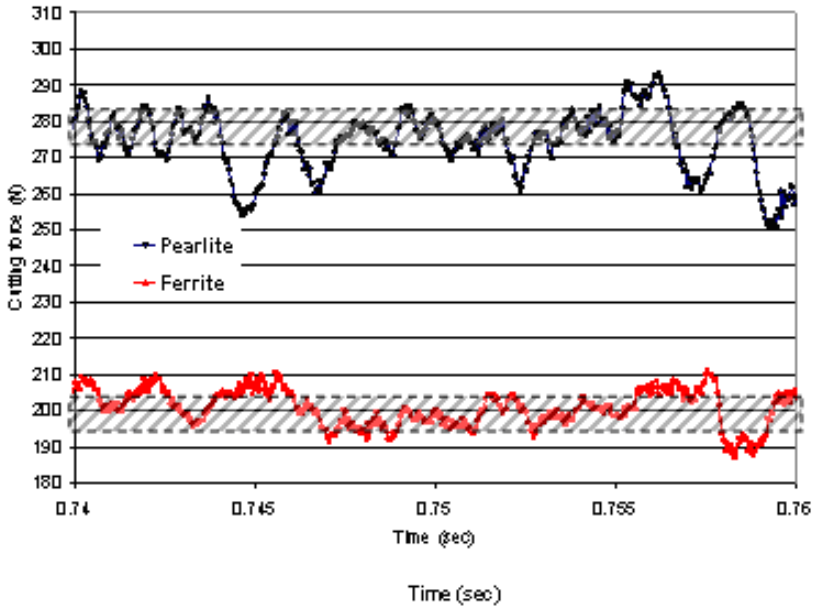

Figure 4.10: Comparison of Cutting Force Fluctuations in Pearlitic and Ferritic Irons on Relatively Large Times Scales

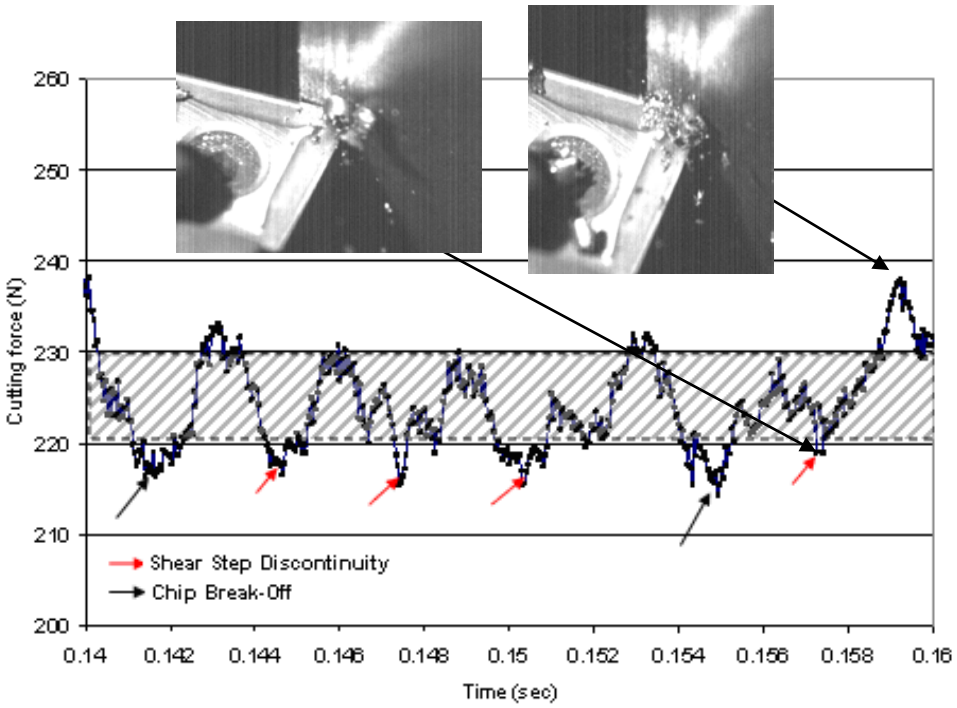

Figure 4.11: Fluctuation of Cutting Force in Ferritic Iron

4.4. ANALYSIS OF MACHINE CHIPS

Machining chips from each face cutting operation were analyzed using tool force data, high-speed videos, scanning electron microscope (SEM), and an optical microscope. From the tool force data plots, it was possible to determine the average time between crack formation allowing for calculation of the distance between cracks. The average distance between the formations of shear step discontinuities (partial crack) for the ferritic irons was nearly double that of the pearlitic irons. Generally the frequency of shear step discontinuity events was significantly higher when compared to the frequency of chip break-off. This was found to be because not all cracks extended deep enough to cause the chips to break-off. Figure 4.12 shows SEM images of the chip internal surface and surface in contact with the rake face of the tool. SEM images of the material in contact with the rake face of the tool were used for evaluation of distances between formations of shear step discontinuities (illustrated by the arrows in the figure). The

average data from these two techniques (tool force and SEM) were similar (Table 4.2). The average lengths of the chips formed from ferritic and pearlitic irons were analyzed both frame by frame from the video and optically measured on collected chips. Both methods indicated slightly larger chip lengths in ferritic iron when compared to pearlitic while the video method indicated large differences of up to 1.1 mm between the two irons.

Table 4.2. Data Analysis Summary of Chip Formation

Micro-structure	Crack Formation			Chip Formation		
	Tool Force		SEM	High-Speed Video		Optical
	Time (sec)	Length (mm)	Length (mm)	Time (sec)	Length (mm)	Length (mm)
Pearlite	0.0018	0.46	0.4-0.5	0.021	5.5	5.0
Ferrite	0.0031	0.81	0.7-1.0	0.027	6.6	5.3

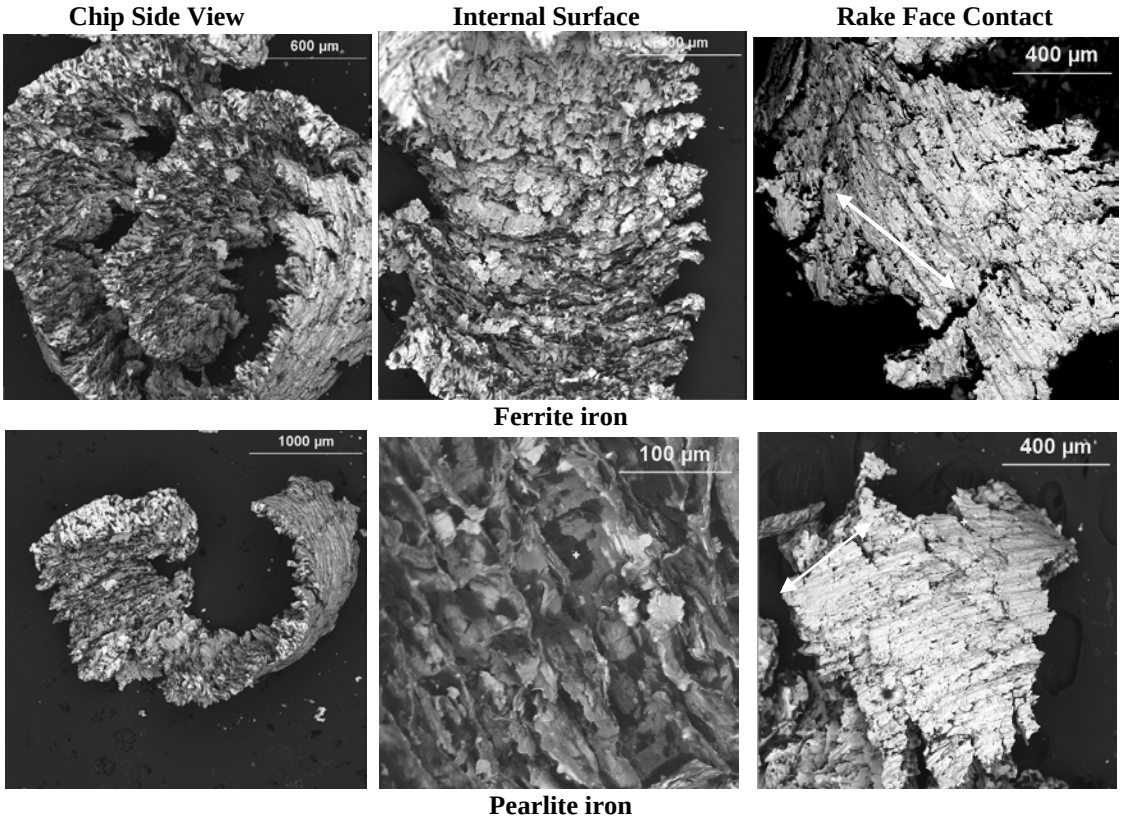

Figure 4.12: SEM Images of Chips Collected from Pearlite and Ferrite Irons

5. EFFECTS OF PHOSPHOROUS AND CHROMIUM

5.1. INDUSTRIAL FOUNDRY SURVEY

Results from the AFS-sponsored foundry survey sent to iron producers indicated that many machinability problems were due to alloy additions or charge material compositions that were just outside of specifications. One of the more common problems for gray cast iron producers was elevated P levels above the max alloy specification. Additionally, P levels on the high-end still within alloy specification in the presence of elevated Cr would also cause increased tool wear/breakage rates. The following experiment was performed in response to the industrial survey to better understand the reason for the decreased machinability that gray cast iron producers were experiencing.

5.2. THERMODYNAMIC MODELING

Figures 5.1 and 5.2 illustrate the effect of alloy content on the eutectic temperature, percent remaining liquid at the eutectic temperature, and the partial composition of the eutectic liquid. In Figure 5.1a it can be seen that as both the wt% P and wt% Cr increase the metastable (carbide) eutectic temperature decreases. With the drop in the eutectic temperature and the assumption of the same cooling rate, a decrease in the graphite flake length is expected to result. In Figure 5.1b, the effect of alloying on the wt% of remaining liquid is shown and it can be seen that as the wt% P alloy added increased the % liquid present at the eutectic temperature also increased. However, as the amount of Cr increased, the % liquid at the eutectic temperature dropped. In this case, the amount of both wt% P and Cr will heavily influence the amount of carbide phase that forms. Finally, in Figure 5.2, the effect of initial alloy content on the composition of the eutectic liquid was evaluated. It was found that as the %P in the melt is increased the amount of P in the remaining liquid increases (as expected), but the amount of carbon in

the remaining liquid decreases. Also in Figure 5.2 the effect of Cr can be seen more clearly. As the amount of alloy Cr increases the level of P in the remaining melt stays constant, but the amount of C in the remaining liquid increases. These conditions suggest that as the Cr levels increase in the presence of P, a more favorable environment for the formation of a phosphide eutectic (steadite) occurs. Additionally, increases in Cr will also tend to increase the percentage of pearlite in the microstructure.

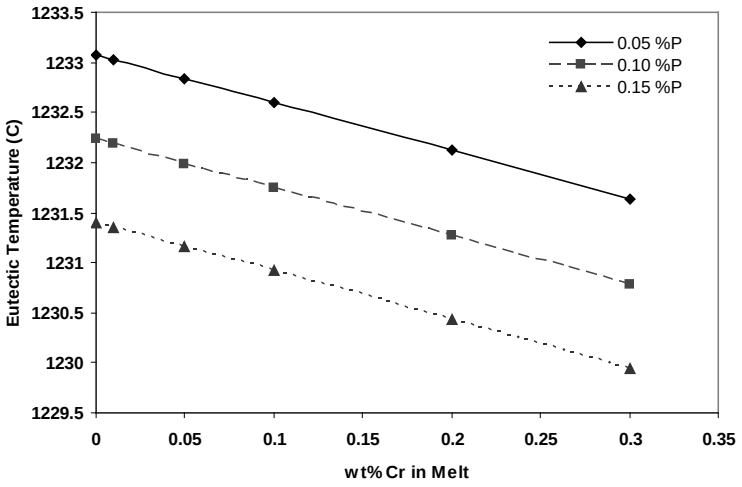

a)

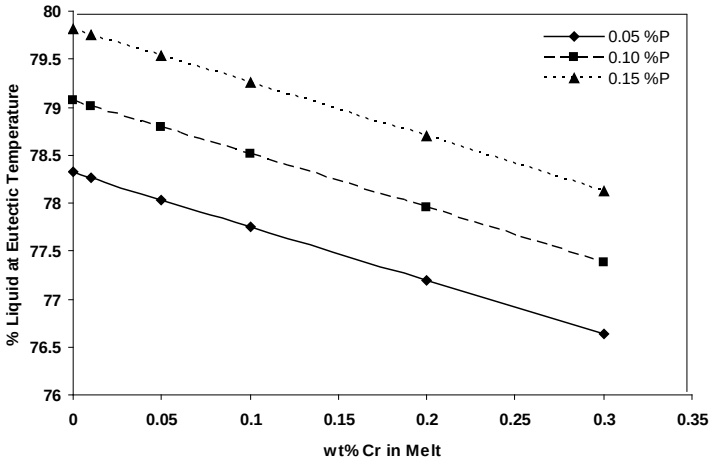

b)

Figure 5.1: Effect of P and Cr on (a) Eutectic Temp and (b) % Liquid

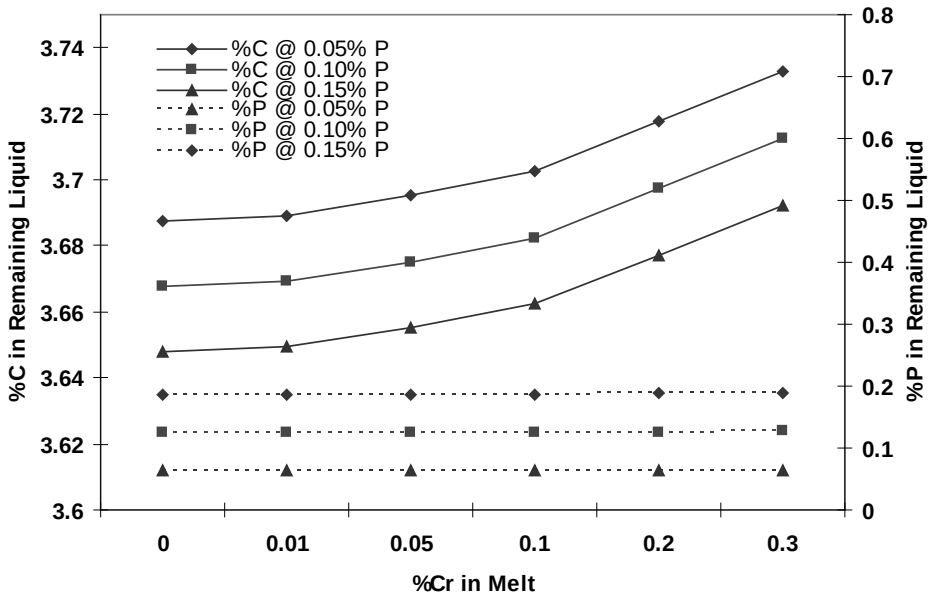

Figure 5.2: C (Left-Axis) and P (Right-Axis) Composition of the Final Liquid

5.3. MACHINABILITY TESTING

Figure 5.3 presents a summary of the average tool force measurements taken during six sequential facing operations for three machinability castings: unalloyed, alloyed with P, and alloyed with both P and Cr. In the figure the cutting force (in N) is plotted against the depth of cut into the casting. The first data point represents a cut 0.380 mm (0.015") deep at the surface of the casting and the following data point represents the same depth of cut 0.380 mm directly beneath the first cut. Therefore, each successive cut progressed further into the "body" of the casting.

The difference in the cutting forces for the initial cut was found to be due to surface roughness. During the casting process, the layer of material solidifying next to the sand mold wall was imparted with a surface texture due to slight metal penetration between sand grains. This surface roughness meant that the initial cut of 0.380 mm in one location could vary up to 0.170 mm, causing the average tool forces to be greater because the average depth of cut was also greater. However, after the first cut the

remaining cuts showed no evidence of texture affecting the measured tool forces. It can be seen that in all cases the cutting forces of the alloyed irons was 10-20 N greater than those of the unalloyed.

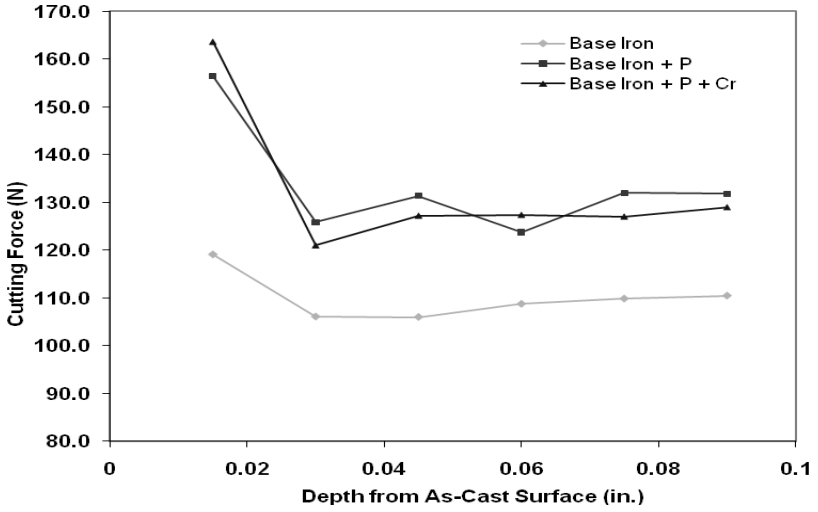

Figure 5.3: Measured Tool Forces for Unalloyed, P-Alloyed, and P+Cr-Alloyed Iron

From the Figure 5.3 data the effect of P on cutting force can immediately be seen, however the effect of Cr is more subtle. At the surface Cr may have an effect on machinability by increasing the cutting forces required, however as the distance away from the as-cast surface increase the effect of Cr is reduced. The machinability behavior of the Cr alloyed iron did not increase cutting forces as greatly. A reason for the minimal response of Cr addition could be due to poor recovery when alloying, but alternatively the effect of slight Cr increases on steadite formation may not be as great as initially observed.

Metallographic examinations were performed in order to evaluate the amount of steadite present in the castings and to examine the effect of Cr on steadite formation. Samples were taken from the same location with regard to the gating system on each casting and polished to a 0.05 micron finish. The metallographic samples were taken from the mid-radius of modified AFS machinability castings and etched with either 2%

nital or Stead's Reagent, chosen to selectively corrode regions low in P contents and distinguish between steadite and Cr-rich carbides. Figure 5.4 below shows micrographs taken from each casting. It can be seen in the unalloyed micrograph that no intergranular phases containing P are present and it is therefore not possible to observe the grain boundaries of the eutectic cells. However, in the alloyed micrographs the grain boundaries are quite prevalent.

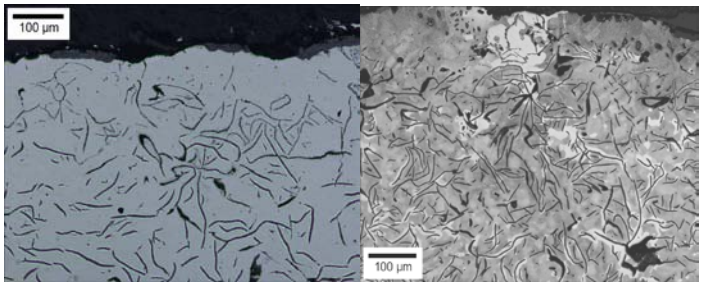

Unalloyed – Unetched Unalloyed – 2% Nital

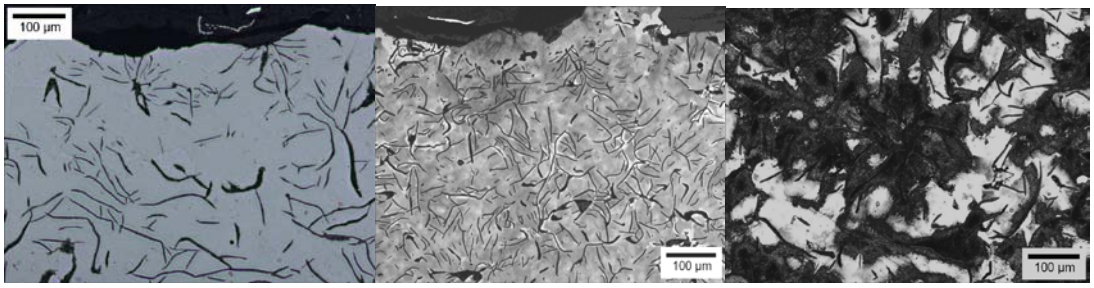

P Alloy – Unetched P Alloyed – 2% Nital P Alloyed – Stead's Reagent

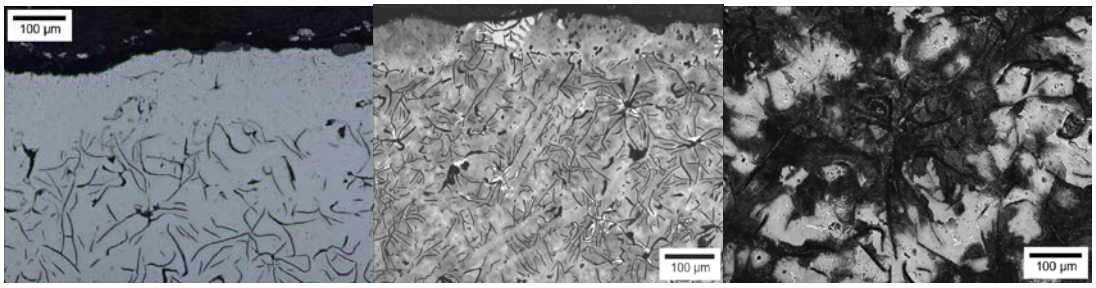

P + Cr Alloy – Unetched P + Cr Alloy – 2% Nital P + Cr Alloy – Stead's Reagent

Figure 5.4: Micrographs from GCI Castings Unalloyed, P Ulloyed, and P+Cr Alloyed

Quantitative metallography of the unetched and etched samples indicated that the overall iron microstructure consisted of Type A flake graphite, with an average flake size of 128 microns (Size 2). The pearlite to ferrite ratios for each sample varied slightly depending on the level of alloy addition, but was between 85-90% pearlitic. The major difference in the microstructures came from the percentages of P. Differences in P bearing steadite phases increased from roughly 14% with alloy P to 19% with alloy P + Cr. Microhardness data indicated that the steadite phase was approximately 315 Vickers greater than the surrounding pearlite/ferrite phases.

6. CASE STUDY: MACHINABILITY EVALUATION OF GCI BRAKE ROTOR

6.1. EVALUATION OF POOR MACHINABILITY CASTINGS

6.1.1. Surface Mapping Results. Castings produced on the old molding line had slightly less variations in the as-cast surface elevations than the castings produced on the old line (reduced tool life, poor machinability). Table 6.1 summarizes the data regarding the total variation. It was found that the good castings had a total surface variation of approximately 0.010-0.020" while the castings of poor machinability had a variation on the order of 0.020-0.030". Microstructural examination and tool force measurements were used to determine that this difference alone was not responsible for the difference in machinability between the two casting sets.

Table 6.1: Summary of Surface Differences

Good Machinability	Difference in Surface Elevation (in.)
G-1	0.0205
G-2	0.0130
G-3	0.0215

Poor Machinability	Difference in Surface Elevation (in.)
B-1	0.0260
B-2	0.0295
B-3	0.0255

6.1.2. Machinability Results. Cutting tool force data indicated that for a 0.015" initial DOC at a cutting speed of 300 sfpm, 180 N was exerted on the tool for the castings of good machinability compared to 175 N for the castings of poor machinability. The cutting force was seen to decrease as the distance from the casting surface increased as shown in Figure 6.1. Table 6.2 summarizes the data from the tool force measurements.

From this data, there is no significant difference between the cutting forces below the surface layer (0.015”). Statistical evaluation of the data presented in Figure 6.1 indicates that all values are within one standard deviation of one another.

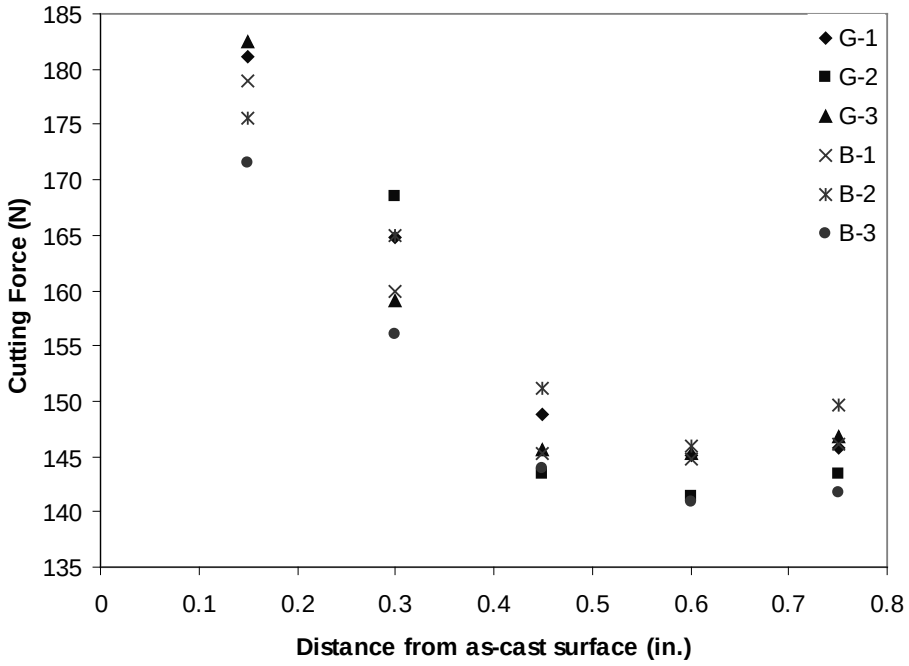

Figure 6.1: Cutting Force as a Function of Distance from As-Cast Surface

Table 6.2: Avg. Cutting Force per Pass in Newtons (N)

Disk	Cut 1	Cut 2	Cut 3	Cut 4	Cut 5
G-1	181	165	149	145	146
G-2	242	169	143	141	143
G-3	182	159	146	145	147
B-1	179	160	145	145	146
B-2	175	165	151	146	150
B-3	172	156	144	141	142

6.1.3. Hardness Testing and Quantitative Metallography. Brinell hardness data, taken for both the casting surface and body, was then compared to the measured cutting forces. In Figure 6.2 it can be seen that the cutting forces near the surface of the casting increase as the brinell hardness decreases while the measured tool forces of the casting body stay relatively constant with decreasing hardness.

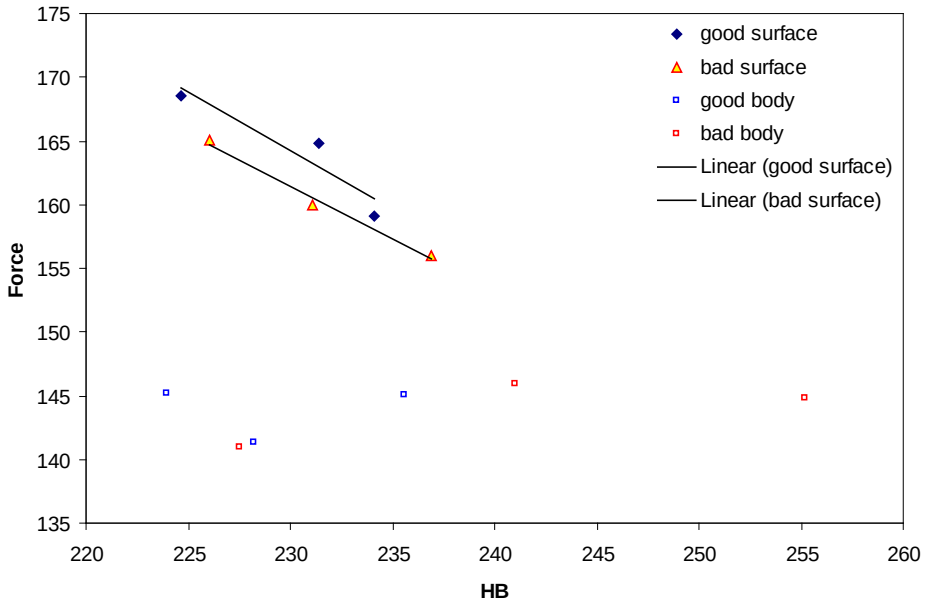

Figure 6.2: Cutting Force vs. Brinell Hardness (Surface and Body) for Cut 2

Metallographic samples from castings of both good and bad machinability were prepared to a 0.05 micron finish and analyzed for graphite type/flake length. Figure 6.3 below compares the unetched surface and body microstructures between the good and bad machinability castings. It was determined from the micrographs that in both cases the castings exhibited a typical type A flake structure with similar flake lengths, but also the presence of small Mn sulfides. The major differences between the castings are the lower number/greater thickness of the graphite flakes and the presence of larger sulfides in the castings of poor machinability. Also the castings of good machinability have a higher tendency for graphite flakes to intersect the casting surface, where the castings of

poor machinability have much less graphite near the as-cast surface. This indicated that a possible surface phase of free-ferrite or carbide was present. From Figure 6.2 a decrease in cutting force was observed, such that the presence of carbide in the near-surface region was unlikely.

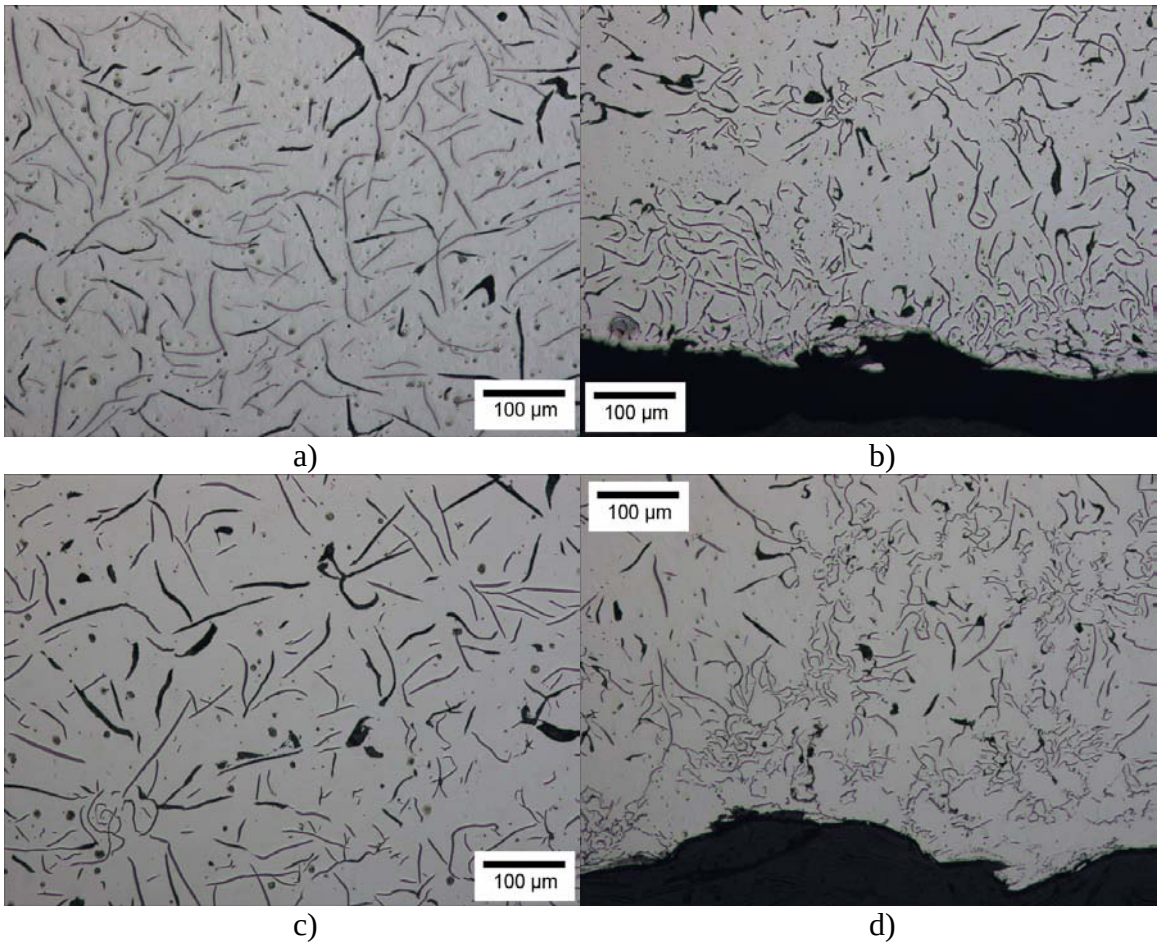

Figure 6.3. Unetched Micrographs: a) Good Machinability Body Microstructure, b) Good Machinability Surface Microstructure, c) Poor Machinability Body Microstructure, d) Poor Machinability Surface Microstructure

All specimens were then etched with a 2% nital solution where the matrix structure was then examined. Figure 6.4 shows that both microstructures contain extremely fine pearlite. Figure 6.5 offers a comparison of the pearlite spacing between the casting sets at 1000x magnification. It is important to note that the castings of poor

machinability also had a higher percentage of free-ferrite (determined by shape and microhardness) at the casting surface compared to those of good machinability.

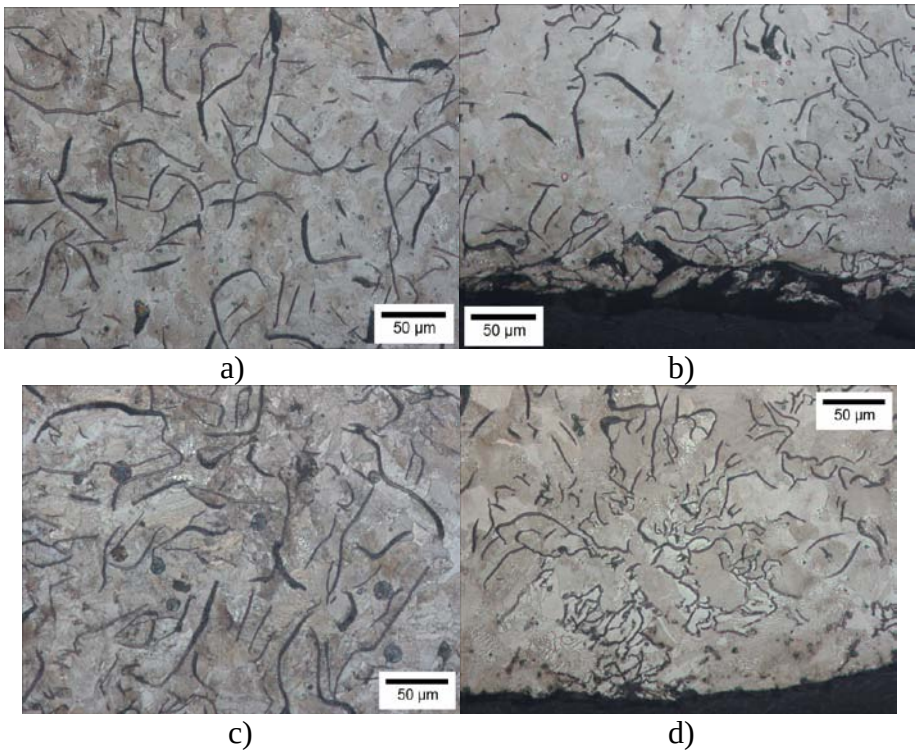

a) b)

c) d)

Figure 6.4. Etched Micrographs: a) Good Machinability Body Microstructure, b) Good Machinability Surface Microstructure, c) Poor Machinability Body Microstructure, d) Poor Machinability Surface Microstructure

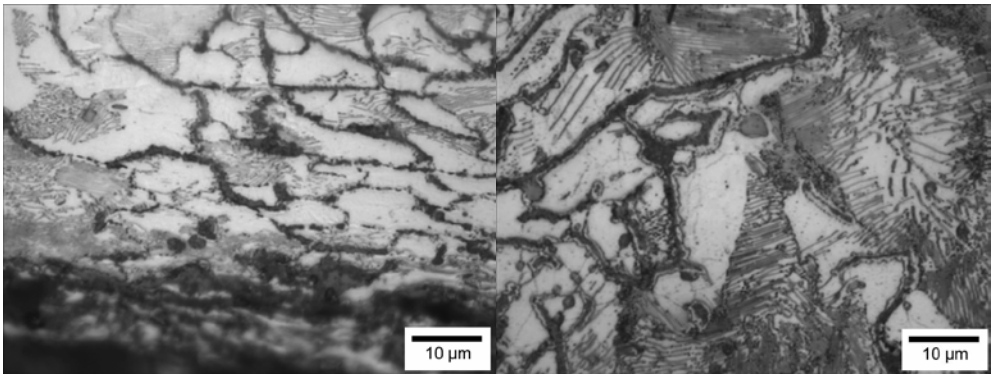

a) b)

Figure 6.5. Pearlite Spacing at Near-Surface: a) Good Machinability Surface Microstructure, b) Poor Machinability Surface Microstructure

Microhardness data was used to identify the surface phase present in both sets of castings. In this process, Vicker's microhardness indentions were made in all of the surface and body phases. It was determined that the white surface phase was harder than graphite, but softer than pearlite. This meant that the phase was most likely free-ferrite as the shape and light color of the phase suggested. If the phase had been carbide the shape would have been much more angular and much harder than pearlite and slightly darker. Figure 6.6 below compares the microhardness of the pearlite in the surface and body microstructures between two castings of good and poor machinability. It can be seen that for all but one case, the surface matrix microstructure was harder than the body matrix microstructure.

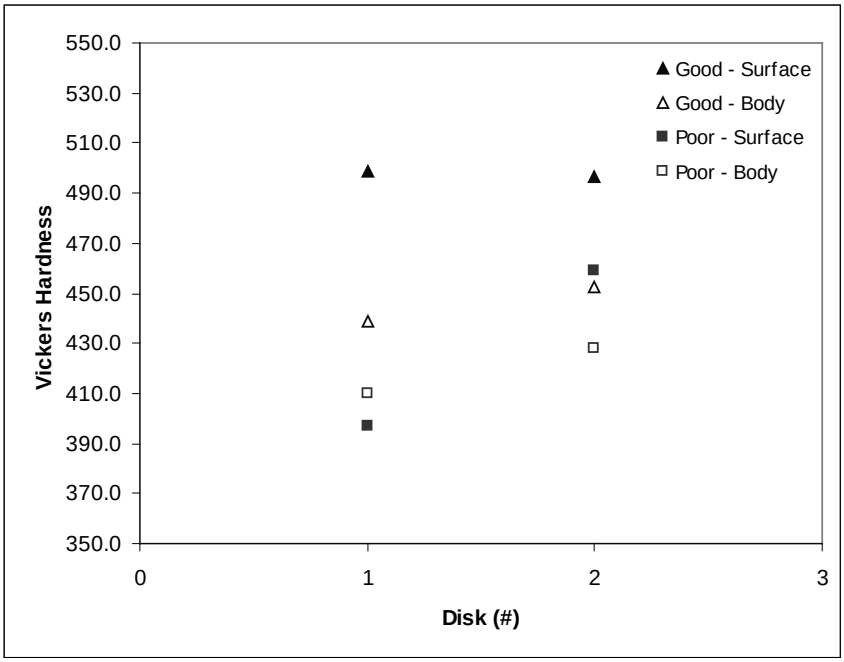

Figure 6.6. Comparison of Vicker's Microhardness Between the Surface and Body Microstructure of Two Sets of Castings

6.2. TESTING OF ALLOY ADDITIONS FOR IMPROVED MACHINABILITY

Figure 6.7 below offers a comparison of the machinability results collected from brake rotor castings with antimony (Sb) added to the original castings analyzed. The antimony addition was intended to reduce the amount of free ferrite in the near-surface region through the stabilization of pearlite. From Figure 6.7 the Sb addition lowered both the specific cutting energy required to machine the as-cast surface and the overall body microstructures with respect to the initial castings provided. However, when compared to castings without Sb produced in the same trial, no significant difference was observed in the machinability data.

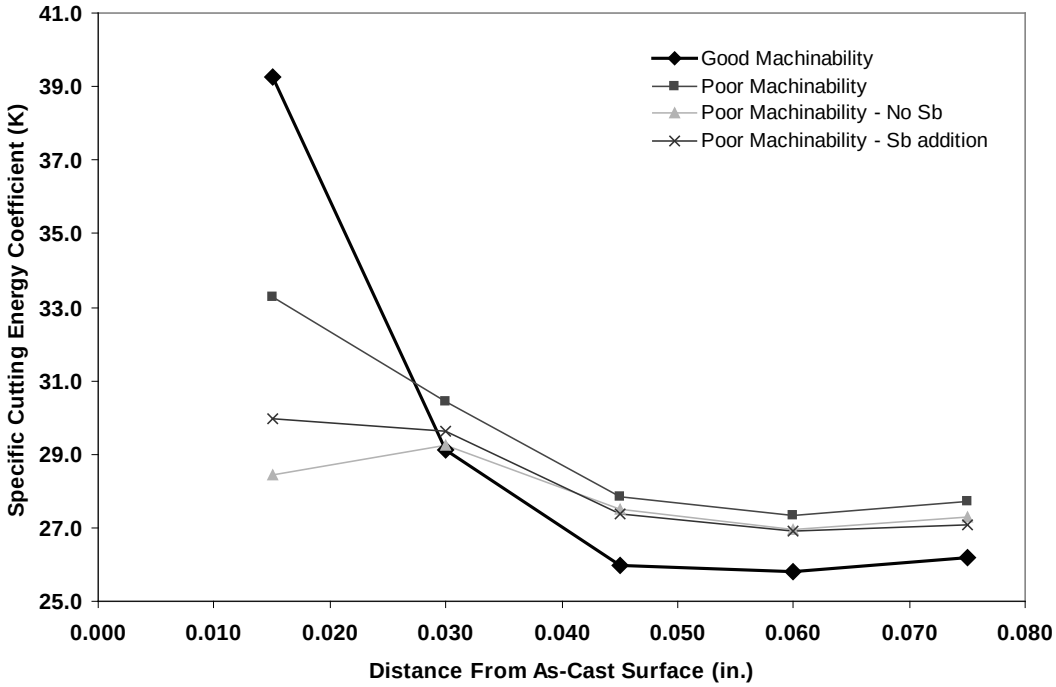

Figure 6.7: Summary of Machinability Data for Castings Produced at Foundry A

The small differences in the cutting forces are not large enough to suggest direct causes for the machinability problems; however the cutting force data suggest that the harder the casting surface, the less energy required to perform a cut. Therefore, the

presence of a soft phase like free-ferrite may be acting to increase the cutting force of the tool insert by sticking to the tool more, causing it to heat up more quickly and not remove as much heat through chip formation processes.

Additions of antimony to the melt to stabilize pearlite formation at the surface were effective in reducing the specific cutting energy, however adjusting cooling rate and inoculation would be more effective ways to solve the surface-free ferrite problem. A newly installed automatic line was found to produce industrial molds of much higher strength and density, than the previous line, and as a result the cooling rates for the castings changed. Additionally, the new green sand used with the new line had not stabilized in properties. It is quite common for green sand systems to take time to become uniform in cooling rate, additive content, and system flow characteristics. Finally, Foundry A was found to use foundry-grade ferro-silicon (a charge material to raise silicon contents) as an inoculant. This practice is not advisable for foundries that use induction melting furnaces because there are not as many "native" inclusions as in cupola melted irons. Induction melted irons require both increased nucleation sites and local CE increase from the dissolving Fe-Si in order to get proper inoculation, which the foundry-grade Fe-Si alone would not provide. This is especially important in the surface regions where nucleation must occur quickly in order to compete with rapid cooling (and solidification) rates. Less effective nucleation will result in less dense graphite flakes structures at the surface while simultaneously raising the Si contents of the surface free ferrite (increasing ferrite strength and hardness).

7. CONCLUSIONS

7.1. MACHINING ALLOWANCE REDUCTION

Based on the following conclusions taken from the machinability experiments regarding near-surface microstructure and machinability, the current machining allowance specifications could be reduced to 0.045-0.060” (1.2-1.5 mm) from a more conservative 0.120-180” (3.0-4.6mm). Assuming that adequate molding, melting, alloy treatment, and microstructure controls are in place, it may be possible to further reduce machining allowance down to 0.035” (0.8 mm).

7.2. EFFECTS ON LABORATORY TEST CASTINGS

1. The near-surface matrix microstructure and graphite flake morphology play a significant role in iron machinability, especially as machining allowances are reduced to accommodate near-net shape casting techniques.
2. The percentage of surface free-ferrite is highly susceptible to changes in graphite flake type/size resulting from inoculation practices and cooling rates. Surface free-ferrite is highly associated with the presence of types E and D graphite.
3. In the presence of soft free-ferrite matrix microstructures, graphite flakes will operate less effectively as chip break-off initiators resulting in larger machine chips forming at slower rates.
4. In the presence of higher percentages of pearlite, graphite flakes will act much more efficiently as chip break-off initiators ahead of the advancing rake face of the tool.
5. In GCI, phosphorus contents above 0.10 wt.% can decrease machinability by creating favorable conditions for iron-phosphide-carbide eutectic (steadite) formation during solidification. This effect worsens with the additional presence of chromium.

7.3. SURFACE EFFECTS ON BRAKE ROTOR CASTINGS

1. The major differences between the castings of good and poor machinability were the surface quality (roughness), graphite flake type/density/thickness, and the presence of free-ferrite.

7.4. FUTURE STUDIES

In order to better understand near-surface machinability it will be necessary to understand which mold-metal chemical interactions specifically alter the near-surface microstructure of gray iron castings, especially in the presence of mold coatings. Furthermore, the effects of mold stability, as-cast surface geometry, and dimensional tolerance over the duration of the solidification/machining process require additional investigation. Finally, as tramp P levels continue to increase in charge materials it may be beneficial to investigate minor alloy additions that render P less effective or methods of stabilizing pearlite without Cr.

BIBLIOGRAPHY

1. *ISO 8062-3,* Geometrical product specifications (GPS) -- Dimensional and geometrical tolerances for moulded parts -- Part 3: General dimensional and geometrical tolerances and machining allowances for castings, 2007.

2. Walton, Charles, F. The Gray Iron Castings Handbook, Gray Iron Founders' Society Inc., 1958, p 495.

3. Cook, N., Jhaveri, P., and N. Nayak. "The Mechanism of Chip Curl and Its Importance in Metal Cutting," *ASME Transactions*, Nov. 1963, p.374-380.

4. Sarma, D. and U. Dixit. "A Comparison of Dry and Air-Cooled Turning of Grey Cast Iron with Mixed Oxide Ceramic Tool," *Journal of Materials Processing Technology*, Vol. 190, 2007, p. 160-172.

5. Schey, John A. Introduction to the Manufacturing Process, McGraw-Hill, Inc. 1987, p446.

6. Berry, J.T. and F.S. Lama. "The Machinability of Ductile Iron," *Industrial Tooling*, 1995, p. 1-19.

7. Trent, E. M. Metal Cutting. Butterworths and Co. Publishing. 1984.

8. Ernst, H., Knowlton, H., Bolton, J., D'Arcambal, A., Bancroft, W., and H. Croft. Machining of Metals, American Society of Metals, 1938, p. 1-34, 77-130.

9. *Williams, J.E. and E.C. Rollason.* "Metallurgical and Practical Machining Parameters Affecting Build-Up Edge Formation in Metal Cutting," *Journal of the Institute of Metals, Vol 98, p. 144, 1970.*

10. Marwanga, R.O. Quality Improvement Through Microstructure Control for Superior Machinability of Cast Irons, Dissertation, Pennsylvania State University, 1998, p. 118-126.

11. Shaw, M.C. "Principles of Material Removal," *Mechanical Behavior of Materials*, Vol. 1, 1979, p. 227-253.

12. Ernst, H. and M. Merchant. "Chip Formation, Friction, and High-Quality Machined Surface, " *ASM Symposium on Surface Treatment of Metals*, 1941, p. 299-335.

13. Degarmo, E., Black, J., and Kohser, R. Materials and Processes in Manufacturing, Wiley and Sons Inc. 2003.

14. Taylor, F. W. “On the Art of Cutting Metals,” *ASME Transactions*, Vol. 28, 1906, p. 31.

15. Zimmerman, C., Boppana, S., and K. Katbi. “Machining of Specific Metals and Alloys: Machinability Test Methods,” *ASM Handbooks – Online*, Vol. 16. 2009.

16. Moore, W. and L. Lord. “Gray Cast Iron Machinability,” *Transactions of the American Foundry Society*, Vol. 67, 1956, p. 193-198.

17. Loria, E. and R. Keller. “A Machinability Test for Treated Cast Iron,” *Iron Age*, Vol. 165, 1950, p.73-76.

18. Souza, J., Nono, M., Oliveira, M., Ribeiro, M., and O. Silva. “Study of Cutting Forces on Machinability Properties of Gray Cast Iron Using New Ceramic Cutting Tools,” *Material Science Forum*, Vol. 591-593, 2008, p. 598-603.

19. Eleftherios,C.V. “Machining Econimics with Phase-Type Distributed Tool Lives and Periodic Maintenance Control,” *Computer Operations Research*, Vol. 23, No. 1, p. 53-62, 1996.

20. Kozochikin, M.P., Kochinev, N.A., and F.S. Sabirov. “Diagnostics and Monitoring of Complex Production Processes using Measurement of Vibration-Acoustic Signals,” Measurement Techniques, Vol. 49, No. 7, 2006, p. 672-678.

21. Boothroyd, Geoffrey and Winston Knight. Fundamentals of Machining and Machine Tools, CRC Press, 2006, p. 79-82.

22. Choudhury, S.K. and K.K. Kishore. “Tool Wear Measurement in Turning Using Force Ratio,” International Journal of Machine Tools and Manufacture, Vol. 40, 2000, p. 899-909.

23. Voigt, R.C., Cohen, P.H., and R.M. Torielli. “Machining of Ductile Irons – Influence of Casting Dimensional Variability on Tool Life Variation,” *Keith Millis Symposium on Ductile Cast Iron*, 2008.

24. Cohen, P.H. “Fundamentals of the Machining Process: Forces, Power, and Stresses in Machining,” ASM Handbooks – Online, Vol. 16, 2009.

25. Black, Paul H. Theory of Metal Cutting, McGraw-Hill, 1961, p. 54-56.

26. White, C.V. “Gray Iron – Flake Graphite Microstructure,” *ASM Handbooks – Volume 1*, 2009.

27. Reed-Hill, R.E. and Reza Abbaschian. Physical Metallurgy Principles, PWS Publishing Company, 1994, p. 590-591.

28. Janowak, J.F. and R.B. Gunlach. “A Modern Approach to Alloying Gray Iron,” Transactions of the American Foundry Society, Vol. 90, 1982, p. 847-863.

29. Loper Jr., C.R. “Inoculation of Cast Iron – Summary of Current Understanding,” Transactions of the American Foundry Society, Vol. 107, 1999, p. 523-528.

30. Davis, J.R. Cast Irons, ASM International Handbook, 1996, p. 32-44.

31. Wallace, J.F., Matijasevic, S., and J. Gomez-Gallardo. “Ferritic Surface Layers on Gray Iron Castings,” Transactions of the American Foundry Society, Vol. 81, 1974, p. 571-591.

32. Wallace, J.F. and G.S. Narasimha Swamy. “Factors Influencing the Ferritic Layer on the Surface of Gray Iron Castings,” Transactions of the American Foundry Society, Vol. 82, 1975, p. 531-550.

33. Mampaey, F. “Solidification mode and feeding behavior of phosphorus alloyed gray cast iron,” *Transactions of the American Foundry Society*, Vol. 111, 2003, pp. 991-1007.

34. Monaghan, B.J., Pomfret, R.J and Coley, K.S., “The Kinetics of Dephosphorization of Carbon-Saturated Iron Using an Oxidizing Slag,” *Metallurgical and Materials Transactions B*, Vol. 29B, 1998, pp. 111-118.

35. Van Niekerk, W.H. and Dippenaar, R.J., “Phosphorus Distribution Between Carbon-Saturated Iron at 1350C and Lime-Based Slags Containing Na_2O and CaF_2” *Metallurgical and Materials Transactions B*, Vol. 29B, 1998, pp. 147-153.

36. Gundlach, R.B. and W.G. Scholz. “Phosphide Eutectic in Gray Cast Iron Containing Molybdenum and/or Chromium,” *Transactions of the American Foundry Society*, 1973, pp. 395-402.

37. Finn, M. “Standard Test for Machinability of Cast Iron – Gray Iron,” Report No. 250-1549-251 (1) of 5-J Quality Control Committee of the American Foundry Society, 2004, p. 1-15.

38. Finn, M. “Putting Iron Machinability to the Test,” Modern Casting, April, 2005, p. 30-31.

39. Li, H., Griffin, R.D., and Bates, C.E., “Effects of Titanium and Filtration on Gray Iron Machinability,” *Transactions of the American Foundry Society*, vol. 113, pp 813-823 (2005).

40. Kahles, J.F., Field, M., “Relation of Microstructure to Machinability of Gray Iron, Ductile Iron, and Malleable Iron,” *Transactions of the American Foundry Society*, vol. 89, pp 587-596 (1981).

41. Pan, E.N., Lin, M.S., and Hong, W.C., “Machinability of Cast Irons with Low Thermal Expansion Coefficient,” *Transactions of the American Foundry Society*, vol. 113, pp 606-623 (2005).

42. Janowak, J.F. and Gundlach, R.B. “Improved Machinability of High Strength Gray Iron,” *Transactions of the American Foundry Society*, 1985, pp. 961-968.

VITA

William Dewey Peach was born on August 1st, 1984 and after completing his education at Rolla High School, entered the Missouri University of Science and Technology (Missouri S&T). He received his Bachelor of Science degree in Nuclear Engineering from Missouri S&T in May 2007 and enrolled for graduate school at Missouri S&T the same year under the Metallurgical Engineering program. He received his Masters of Science degree in the fall semester of 2009 and is currently employed by Los Alamos National Laboratory.